NIMBUS-7 OBSERVATIONS OF THE EFFECT OF CLOUDS ON THE EARTH'S RADIATION BUDGET

Thomas J. Greenwald
Graeme L. Stephens
Thomas H. Vonder Haar

CIRA Cooperative Institute for Research in the Atmosphere

Colorado State University

Nimbus-7 Observations of the Effect of Clouds on the

Earth's Radiation Budget

Thomas J. Greenwald, Graeme L. Stephens and Thomas H. Vonder Haar

CIRA Report – August 1990

U18400 9372064

ABSTRACT

Outgoing longwave (LW) flux and shortwave (SW) albedo data obtained from narrow field-of-view scanner measurements aboard the Nimbus–7 satellite are used along with coincident cloudiness data to estimate the effect of clouds on the earth's radiation budget (ERB). A simple techique is described to obtain clear sky albedos and LW fluxes using daily Nimbus–7 ERB and total cloud amount data. The analysis is done for the following four seasons: June-August 1979, September-November 1979, December-February 1980, and March-May 1980. When compared with the recent results from the Earth Radiation Budget Experiment (ERBE) the Nimbus–7 derived clear sky LW and SW fluxes are about 5–6 Wm^{-2} too low and 3–4 Wm^{-2} too high, respectively, most likely resulting from cloud contamination.

The concept of cloud radiative forcing, referred to in this study as cloud effect, can provide a quantitative measure of the impact of clouds on the ERB. It is defined as the difference between the clear sky flux and the cloudy sky flux at the top of the atmosphere. The SW cloud effect is shown to be negative over most of the earth and is greatest in the midlatitudes in areas of stratus clouds and storm tracks. The LW cloud effect, on the other hand, is primarily positive and most significant in the tropics. The net cloud effect is found to be negative over most of the earth, with a near cancellation of the SW and LW effects in the tropics and a significant negative effect in the midlatitudes. Moreover, it is shown that the net cloud effect, when globally averaged, is negative and varies with season. A comparison of the Nimbus–7 derived LW and SW cloud effects to those obtained from ERBE shows, on average, a 5–6 Wm^{-2} bias resulting from cloud contamination of the Nimbus–7 clear sky fluxes.

TABLE OF CONTENTS

1. Introduction

A topic that has recently gained considerable attention is the role that clouds play in climate and climatic change. Although it has long been recognized that clouds influence climate through modification of the earth's radiation budget (ERB) and hydrologic cycle, their impact on climate is not well understood. Clouds can significantly affect the ERB at the top of the atmosphere and the surface by altering the amount of solar radiation that reaches the ground, and by their absorption and emission of upwelling longwave radiation from the earth's surface. Therefore, from a radiative heating point of view, clouds produce two opposing effects. In the solar spectrum they tend to cool the earth and in the infrared spectrum they cause the earth to warm. Furthermore, it is the radiative heating/cooling caused by clouds that directly affects the general circulation of the earth's atmosphere and oceans.

Several major programs are now in progress that are devoted to increasing our knowledge of the relationships between clouds, the ERB, the hydrologic cycle, and climate. One such program is the International Satellite Cloud Climatology Project (ISCCP). ISCCP is a five year project (beginning in July 1983) that involves the collection of satellite data from many different sources in order to produce a global climatology of the radiative characteristics of clouds (Schiffer and Rossow, 1983). One aspect of ISCCP will involve an investigation of the interrelationship of clouds and the ERB and hydrologic cycle. The Earth Radiation Budget Experiment (ERBE) is another major project (which began in November 1984) that seeks to measure the ERB at the top of the atmosphere using a multiple satellite system (Barkstrom, 1984). Some of the objectives of ERBE are to determine the monthly average radiation budget on regional, zonal, and global scales, and to investigate the diurnal variability of the radiation budget.

The specific aims of this study are, first, to present a method of deriving clear sky longwave (LW) and shortwave (SW) radiative fluxes from Nimbus-7 observations so that the direct effects of clouds on the ERB may be estimated. Second, the clear sky fluxes and cloud effect results from Nimbus-7 are compared to those from ERBE in a zonally and globally averaged sense. In the first part of this study a description of the ERB and cloud amount data sets is given. This is followed in

1

section 3 by a discussion of the methods used in obtaining clear sky LW and SW fluxes, including an estimate of the errors involved in these methods. The derived clear sky SW, LW, and net fluxes are depicted as color global maps and their basic features are discussed. In addition, they are compared to the clear sky fluxes available from ERBE. The fourth section includes a discussion of the global maps of SW, LW, and net cloud effect derived from Nimbus–7 observations, and these results are also compared to ERBE data on a zonally and globally averaged basis. Finally in section 5, the conclusions that were drawn from this study are presented.

2. Data Sources

2.1 Earth Radiation Budget Data

The primary source of ERB data used in this study were processed from radiance measurements taken by the narrow field-of-view (NFOV) scanning radiometer on board the near-polar orbiting Nimbus–7 satellite. The satellite was launched on October 24, 1978 and several experiments aboard the satellite continue to take observations. The NFOV scanner was designed to operate for roughly one year, providing measurements for 19 months until June 22, 1980 (Jacobowitz et al., 1984). The scanner consists of four telescopes that measure both outgoing LW radiance in a broad band from 4.5 μm to 50 μm and reflected SW radiance from 0.2 μm to 4.5 μm.

The outgoing LW fluxes at the top of the atmosphere (TOA) were computed from the scanner radiance measurements using a simple angular distribution model to describe the limb characteristics of the radiation field (Jacobowitz et al., 1984). The conversion from SW radiance measurements to fluxes is more complex and involves four angular distribution models based on Nimbus–3 observations representing different surface types (Raschke et al., 1973). In the second step of the processing, the daily average LW flux is determined from a weighted average of the ascending and descending-node observations and the daily average SW albedo is found from models that correct for the diurnal variation of albedo (Arking and Vemury, 1984). It is not possible to provide an accurate assessment of the uncertainties in the processed SW and LW fluxes. A reasonable,

2

conservative estimate of this error on a regional scale is about 10 Wm^{-2} for SW fluxes, while the uncertainty in the LW fluxes is probably somewhat less.

The daily average NFOV LW flux and SW albedo data sets are spatially distributed on an equal area world grid that consists of 2070 boxes (or targets) each approximately 500 km by 500 km in size. Because of the three-day-on and one-day-off operation of the scanner, the number of days of data for each month varies from 21 to 24 days.

The data provided by ERBE are the secondary source of ERB data used in this study and represent the state of the art in ERB data. Measurements from three satellites are used in the ERBE. These include the Earth Radiation Budget Satellite (ERBS), which was launched Oct. 5, 1984 and is in a low inclination orbit, and two sun-synchronous satellites, NOAA-9 (launched Dec. 12, 1984) and NOAA-10 (launched Sept. 17, 1986). Each satellite has a NFOV scanner package consisting of three telescopes that detect outgoing reflected SW radiance from 0.2-5 μm, broadband LW radiance in a range of 5-200 μm and the total radiance from 0.2-200 μm.

The processing of ERBE LW and SW radiances into fluxes involved the use of many angular distribution models for various cloud conditions and surface types. These models were developed, primarily, from Nimbus-7 observations (Barkstrom, 1984). Temporal averages of the processed LW and SW fluxes are provided in the form of daily averages, monthly averages of the daily averages, and averages of the monthly hourly averages on a 2.5° grid. In this study, the ERBE monthly average of the daily averages data is used. Preliminary results of the estimated rms uncertainty of the processed total fluxes on a regional scale are about 5 Wm^{-2} for the SW and 3 Wm^{-2} for LW fluxes. These uncertainties are due, largely, to misclassification of scene types (Harrison *et al.*, 1990).

Unlike the Nimbus-7 ERB data set, clear sky fluxes are included as a standard product of the ERBE processing system. The LW and SW clear sky fluxes provided by ERBE are found to be biased high by about 4 Wm^{-2} and 1 Wm^{-2}, respectively, based on a regional scale and monthly mean (Harrison *et al.*, 1990).

3

2.1 Cloudiness Data

The cloud amount data used in this study were inferred from observations taken by the Temperature Humidity Infrared Radiometer (THIRS) and Total Ozone Mapping Spectrometer (TOMS) also aboard the Nimbus–7 satellite. This was accomplished through a bispectral algorithm described in detail by Stowe *et al.*, (1988). THIRS is a two-channel radiometer that measures emitted LW radiance at 6.7 μm and 11.5 μm bands. Only the 11.5 μm channel measurements are used in the infrared (IR) cloud algorithm. The TOMS instrument measures reflected ultraviolet (UV) radiance at six different wavelengths in a range from 0.313 to 0.380 μm. The UV cloud algorithm uses the average of the UV reflectivities computed from measurements at 0.360 μm and 0.380 μm.

For the case of the IR algorithm, THIRS measurements are used to determine if a given field-of-view (FOV) is cloudy or clear based on radiance thresholds. These thresholds are obtained, in part, from Air Force 3-D surface temperature analysis. This information is then used to find cloud amount over a subtarget area (165 km by 165 km). The UV algorithm, on the other hand, infers total cloud amount for each FOV using TOMS computed reflectivities, based on a linear relationship between total cloud amount and UV reflectivity. The average reflectivities of all FOV's within a given subtarget area are then used to determine the cloud amount in that subtarget area. From these two independent estimates of total cloud amount, a bispectral algorithm (daytime only) is then applied to determine a single combined cloud amount estimate.

The uncertainties in the total cloud amount estimates from the bispectral algorithm were determined by comparing them to estimates of total cloud amount from an analyst's interpretation of nearly coincident geostationary satellite images, along with corresponding meteorological surface observations. When compared with the analyst estimates it was found that the systematic errors in total cloud amount were less than 10% and random errors ranged from 7 to 16% (Stowe *et al.*, 1988).

4

The total cloud amount data are directly used in this study to aid in estimating clear sky Nimbus-7 ERB fluxes. The data are distributed on the same equal area world grid as the ERB data and represent an average of the ascending and descending-node total cloud amount estimates.

3. Clear Sky Analyses

3.1 Procedure

A technique to estimate clear sky LW and SW fluxes from Nimbus-7 ERB data was proposed by Ardunay, *et al.* (1988, 1989). The LW method involved the use of a linear regression between daily outgoing LW flux and total cloud amount. However, the dependence of the LW flux on cloud height was also taken into account. This was accomplished by converting separately the clear and cloudy sky fluxes to equivalent black body temperature using THIR 11.5 μm window radiances for cloudy and clear areas. Then a relationship between these window radiances and ERB broadband scanner radiances, developed by Ohring *et al.* (1984), was applied. The SW method, on the other hand, consisted of a linear regression between daily broadband albedo and total cloud amount. The optical depth of the cloud was accounted for by assuming it was proportional to the difference between the clear sky and cloud top temperatures.

The approach devised for this study to estimate clear sky fluxes, in contrast to the technique mentioned above, was less complicated. The method used to estimate clear sky SW albedos was to apply a 20% cloudiness threshold to the daily ERB data and use the minimum albedo below this threshold as the clear sky value. It was found that a 20% threshold provided the most satisfactory results. A higher threshold increased the effect of clouds on the albedo and, likewise, a lower threshold reduced the number of areas with a clear sky value. The minimum albedo method works well over most areas of the earth except for regions viewed at low sun angles and covered by bright snow and ice. Under these conditions it is possible for very thick clouds to appear less reflective than the surface (Ellis, 1978). Therefore, the clear sky albedos determined from this method may be suspect in winter polar regions. The clear sky LW fluxes were estimated

Table 1: Standard deviations of the clear sky LW and SW (in parentheses) fluxes (in Wm^{-2}) obtained from the analysis of Nimbus-7 ERB data described in the text.

Season	Ocean	Land	Globe
JJA	5.4 (10.6)	8.0 (10.8)	6.7 (10.7)
SON	6.9 (10.2)	9.0 (11.0)	7.9 (10.6)
DJF	7.2 (10.4)	9.1 (10.0)	8.1 (10.2)
MAM	6.9 (9.0)	9.6 (11.9)	8.2 (10.4)
Annual	6.6 (10.1)	8.9 (10.9)	7.7 (10.5)

by applying the same cloudiness threshold technique used for the SW albedos, except that the average flux was computed below the threshold.

A seasonal analysis of the Nimbus–7 ERB data was chosen over a monthly one because it was somewhat common, in the tropics for instance, for the total cloudiness to be greater than 20% for an entire month. Yet, even from the seasonal analysis there were some regions left without a clear sky value. In order to retain a simple analysis there was no attempt made to develop an algorithm to fill in these areas. The analysis was done for the seasons of JJA 1979, September-November (SON) 1979, December-February (DJF) 1980, and March-May (MAM) 1980. The number of days of data varied for each season with SON 1979 and MAM 1980 each represented by 68 days, DJF 1980 with 67 days, and JJA 1979 with 69 days.

A crude estimate of the uncertainties in the Nimbus–7 clear sky SW and LW fluxes may be obtained by calculating the standard deviation σ. These uncertainties are largely a result of the sample size, cloud contamination and the natural seasonal fluctuations of the clear sky flux. Since the clear sky albedos were determined from a single minimum value, the standard deviation was estimated from the six lowest albedos for less than 20% cloudiness over the course of a month. One problem with computing the standard deviation in this way is that it will tend to inflate σ, resulting from the small sample size of six data points or less. The clear sky LW flux σ, on the other hand, was computed from all fluxes below 20% cloudiness for the month. Table 1 shows the seasonal and annual clear sky SW and LW flux standard deviations σ over land, ocean and the globe. The LW σ is typically about 7 Wm^{-2} over the ocean and 9 Wm^{-2} over land. For the SW σ there is somewhat less difference between land and ocean with a value of about 10 Wm^{-2}.

Upon comparison of the wide FOV measurements with those from the NFOV scanner, it was discovered that the computed NFOV shortwave albedos were approximately 10% too high (Arking and Vemury, 1984). Although this discrepancy was attributed to scene identification problems, it instead was most likely related to a problem in the original calibration of the scanner (G. Campbell, private communication). Thus, the albedo data used in this study were multiplied by a factor of

7

0.9 to account for this apparent bias. In addition to the bias there were some cases of albedos greater than 1.0 near the winter polar regions (Tighe and Shen, 1984).

3.2 Results

Global maps of clear sky albedo, LW flux, and net flux are presented, for the four seasons described earlier, in the form of cylindrical equidistant projections. In these maps gray areas denote grid boxes where there is insufficient information to obtain a clear sky quantity.

The global fields of clear sky albedo, derived from the minimum albedo method described in the previous section, are shown in Figures 1 and 2. What is most evident from these figures is that the lowest albedos are associated with the oceans, with a typical value of about 10%. As expected, the highest albedos occur in and around the polar regions as a result of the high reflectivity of snow and ice. The effect of snow on surface albedo can be seen dramatically in the northern hemisphere winter (DJF 1980) in Figure 2a, where the high albedos throughout most of northern Asia and North America are due to the snowpack. Over land, the highest albedos occur in desert areas and the lowest over the tropical rainforests of South America and Africa. The effect of cloud contamination on the clear sky albedo can be seen in the northern Pacific and Atlantic oceans and in the southern midlatitudes. In addition, the effects from stratocumulus clouds off the western coasts of South America and Africa can be seen in Figures 1a and b for JJA 1979 and SON 1979.

The global distribution of clear sky LW fluxes are depicted in Figures 3 and 4. The highest LW fluxes occur in the tropics and subtropics, with maxima in desert regions over land and in areas over the ocean where subtropical high pressure systems exist. As expected, the lowest longwave fluxes occur in the polar regions.

The clear sky net flux is simply the difference between the absorbed SW flux and the outgoing LW flux:

$$F_{net,clr} = \frac{S_o}{4}(1 - \alpha_{clr}) - F_{clr}, \tag{1}$$

where F_{clr} and α_{clr} are the respective clear sky LW flux and SW albedo at the TOA. S_o is the solar insolation at the TOA, which depends on latitude and the time of the year. From Figures

8
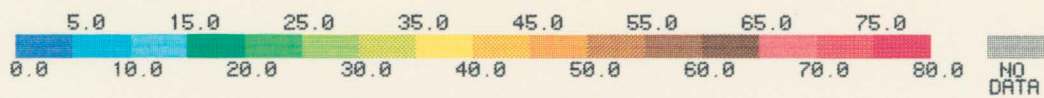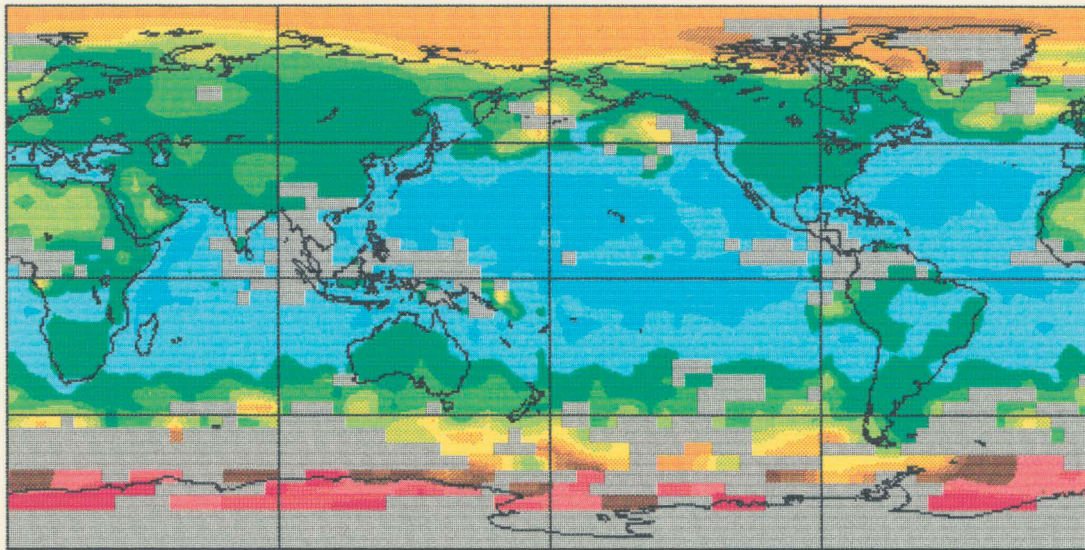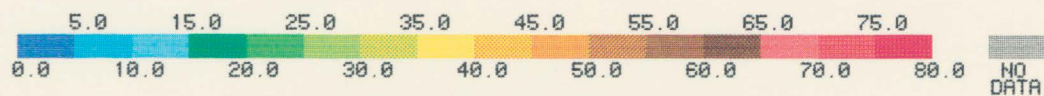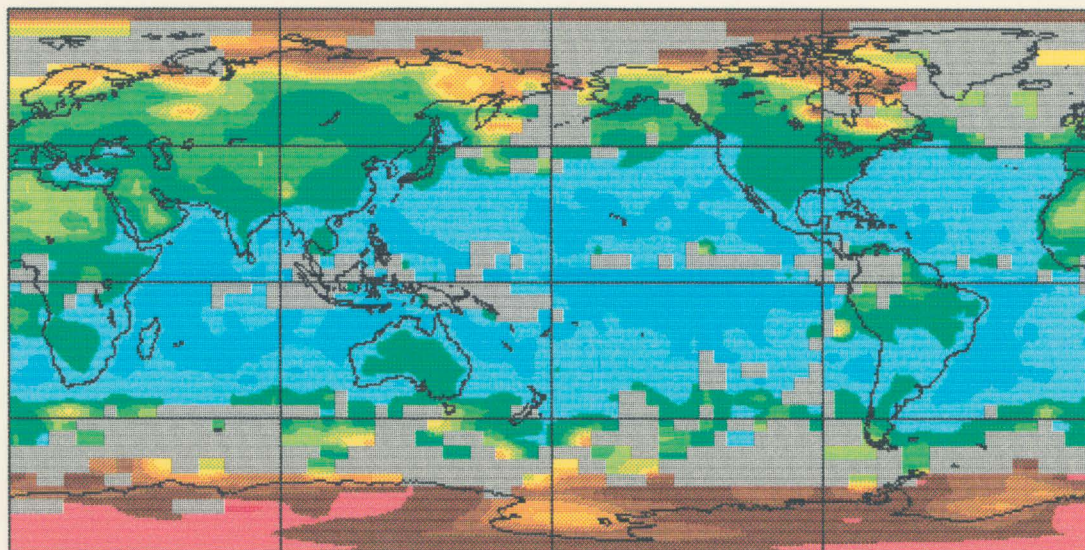
Figure 1. Global distributions of clear sky albedo (%) for (a) JJA 1979 and (b) SON 1979.
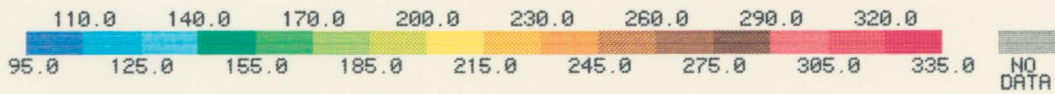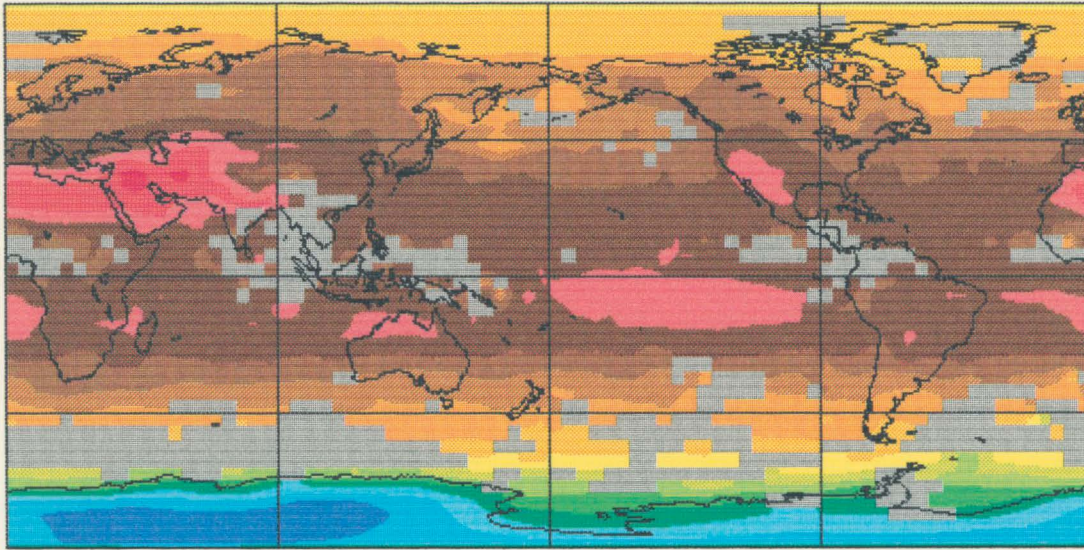
a
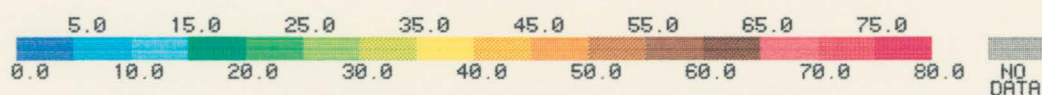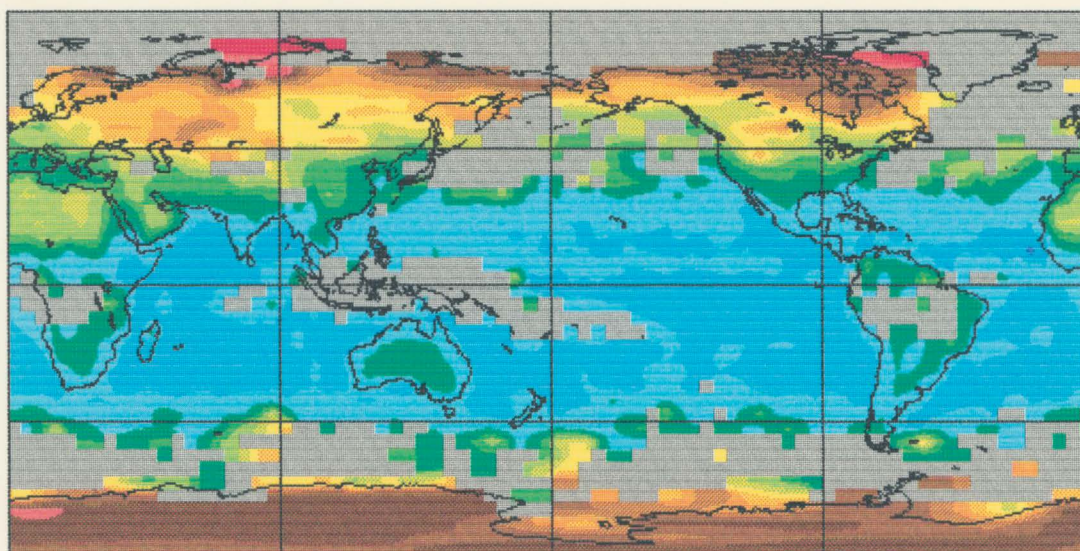
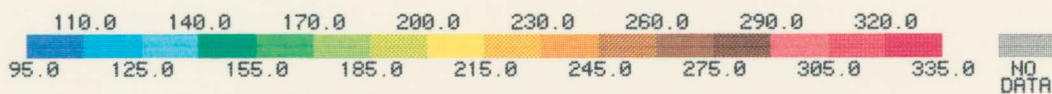CLEAR SKY ALBEDO (%)
DJF 1980

b
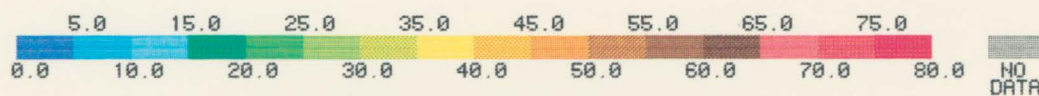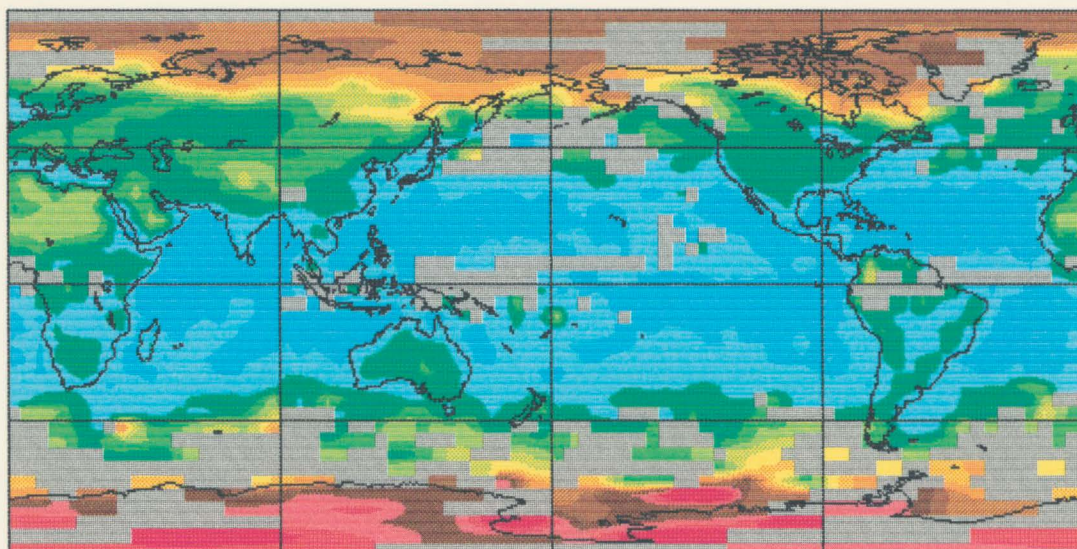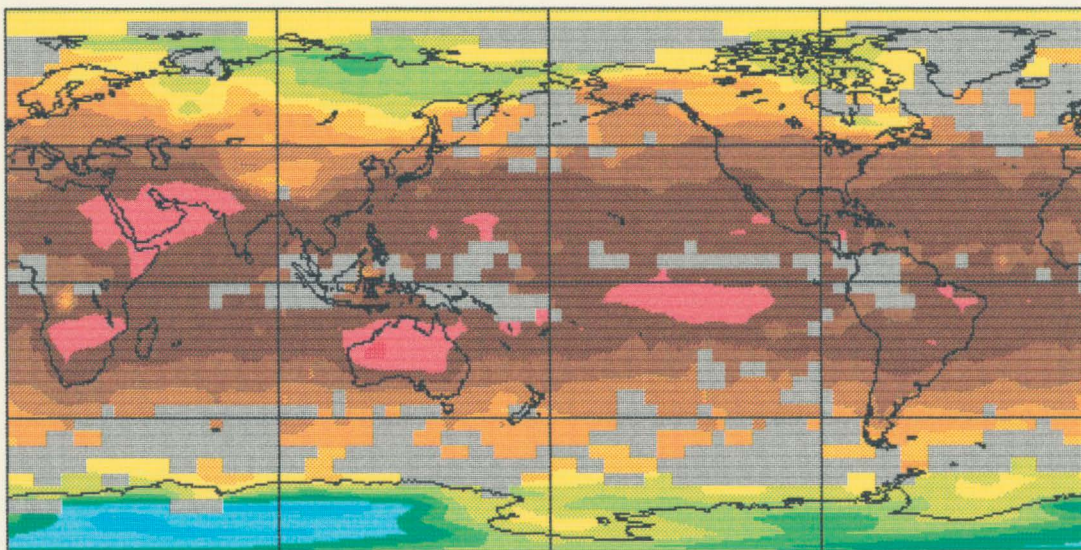
CLEAR SKY ALBEDO (%)
MAM 1980

Figure 2. Same as Fig. 1 except for (a) DJF 1980 and (b) MAM 1980.
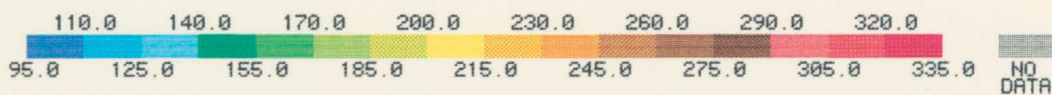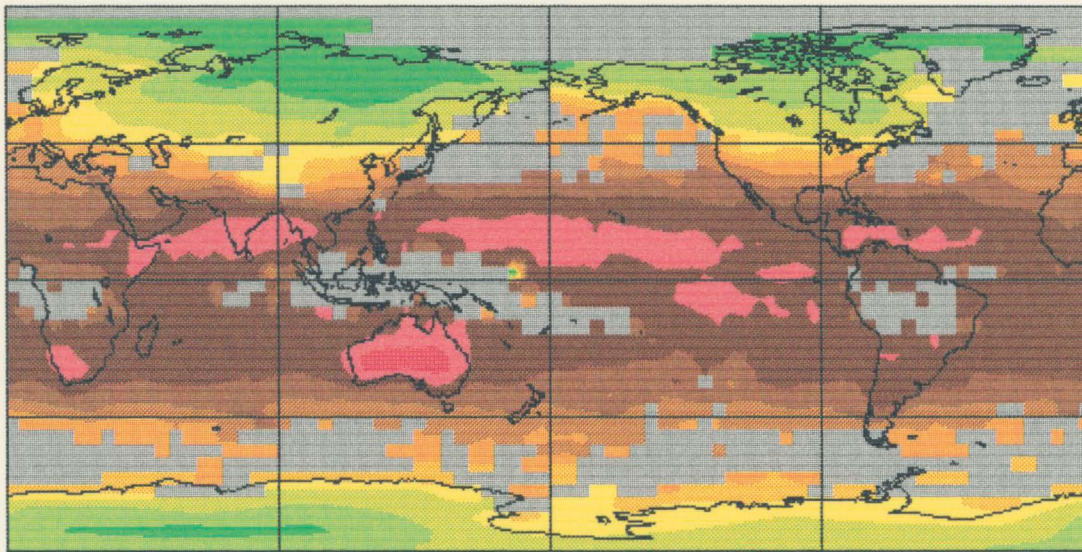
a

CLEAR SKY LW FLUX (W/M**2)
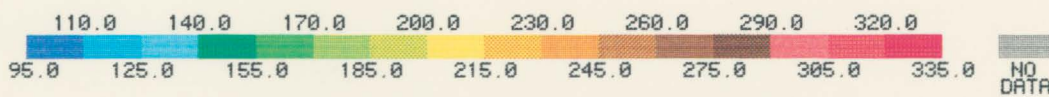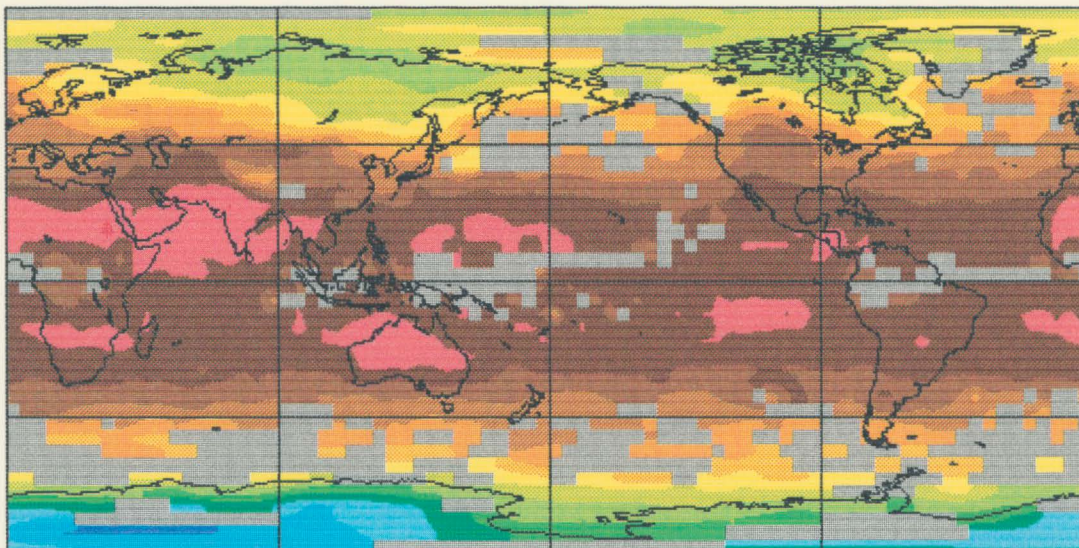JJA 1979

b

CLEAR SKY LW FLUX (W/M**2)
SON 1979

Figure 3. Global distributions of clear sky LW flux (Wm^{-2}) for (a) JJA 1979 and (b) SON 1979.
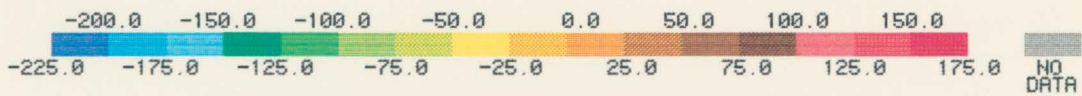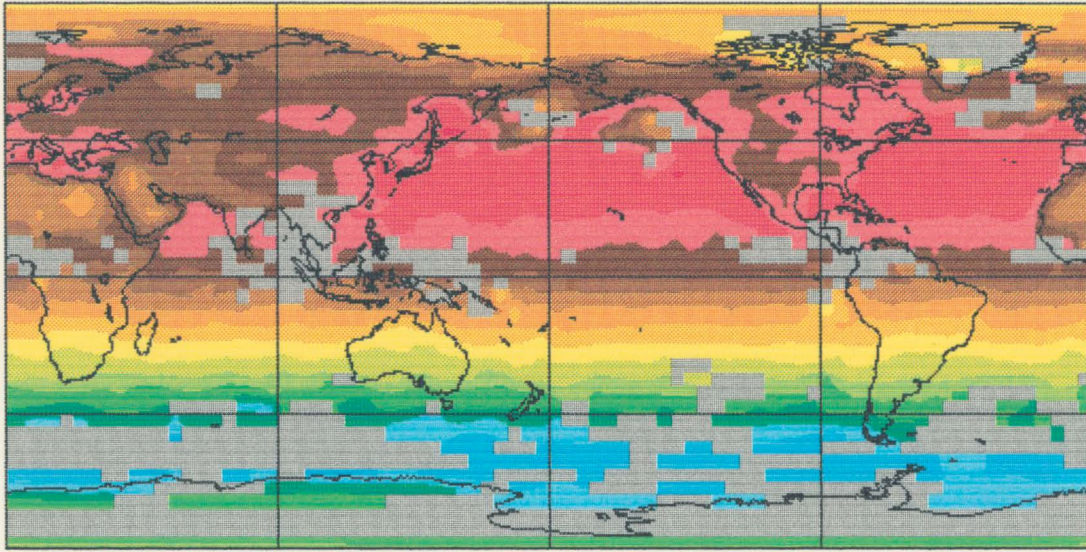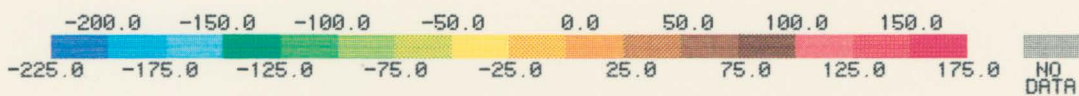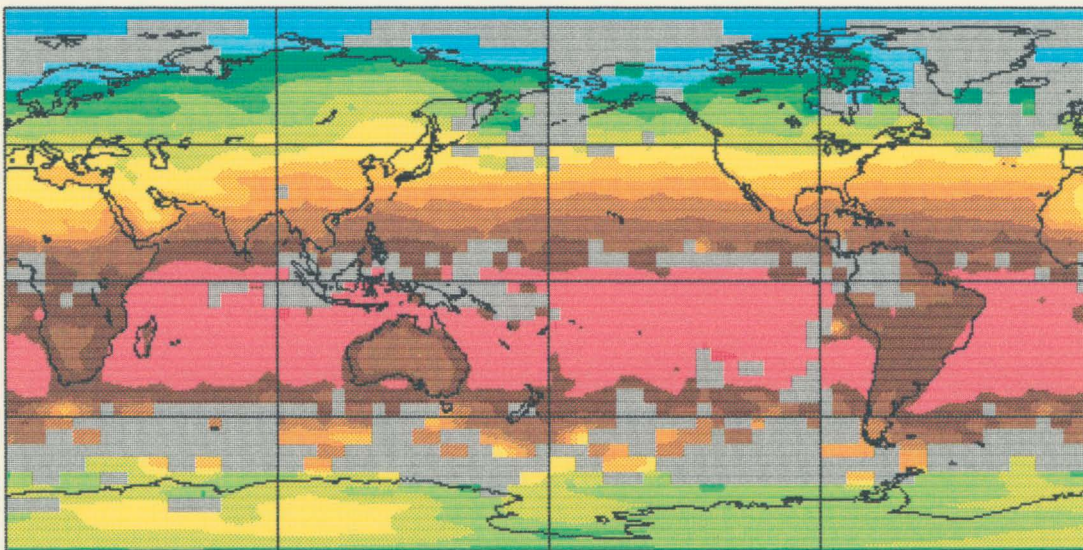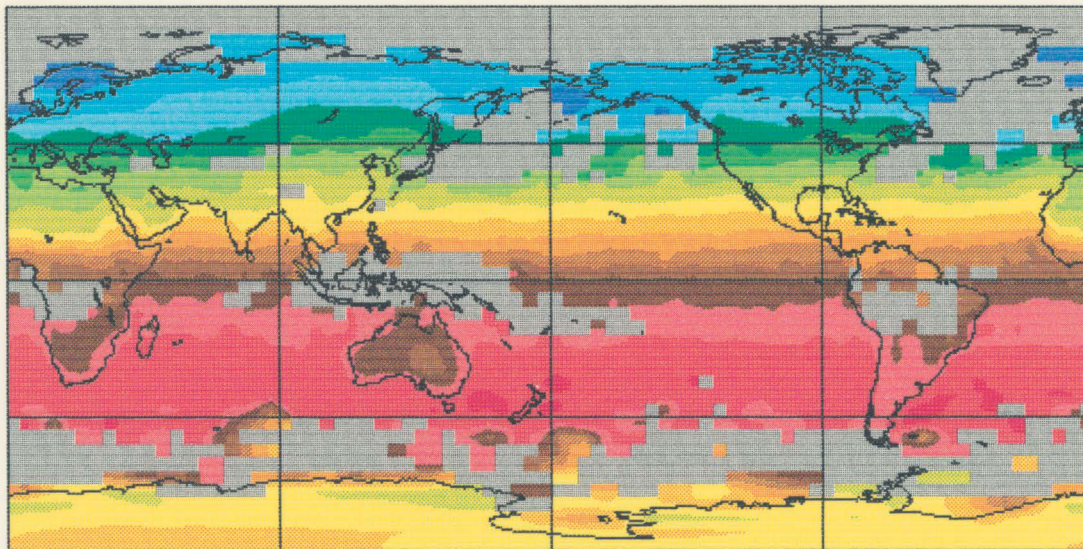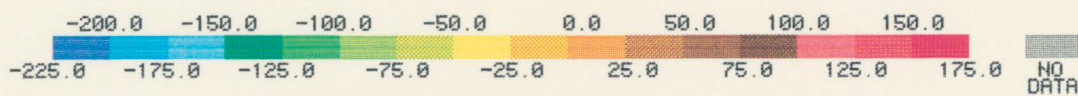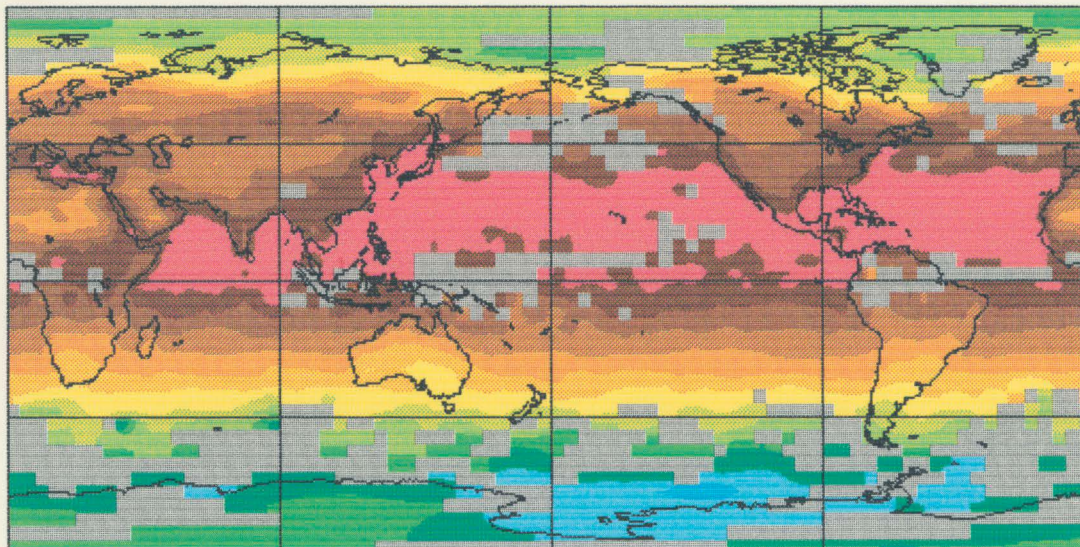
CLEAR SKY LW FLUX (W/M**2)
DJF 1980

b

CLEAR SKY LW FLUX (W/M**2)
MAM 1980

Figure 4. Same as Fig. 3 except for (a) DJF 1980 and (b) MAM 1980.

a

-200.0   -150.0   -100.0   -50.0   0.0   50.0   100.0   150.0
-225.0   -175.0   -125.0   -75.0   -25.0   25.0   75.0   125.0   175.0   NO DATA

CLEAR SKY NET FLUX (W/M**2)
JJA 1979

b

-200.0   -150.0   -100.0   -50.0   0.0   50.0   100.0   150.0
-225.0   -175.0   -125.0   -75.0   -25.0   25.0   75.0   125.0   175.0   NO DATA

CLEAR SKY NET FLUX (W/M**2)
SON 1979

Figure 5. Global distributions of clear sky net flux (Wm^{-2}) for (a) JJA 1979 and (b) SON 1979.

a

-175.0   -125.0   -75.0   -25.0   25.0   75.0   125.0   175.0
-200.0 -150.0 -100.0 -50.0   0.0   50.0   100.0   150.0   200.0   NO DATA

CLEAR SKY NET FLUX (W/M**2)
DJF 1980

b

-200.0   -150.0   -100.0   -50.0   0.0   50.0   100.0   150.0
-225.0 -175.0 -125.0 -75.0   -25.0   25.0   75.0   125.0   175.0   NO DATA

CLEAR SKY NET FLUX (W/M**2)
MAM 1980

Figure 6. Same as Fig. 5 except for (a) DJF 1980 and (b) MAM 1980.

14

5 and 6 it can be seen that the clear sky net flux is, for the most part, zonally uniform over the oceans. Over land it is more variable because of variations in land surface properties. The net flux is greater over the ocean than over land since the lower albedo of the oceans allows greater absorption of incoming solar radiation.

As a verification for the clear sky fluxes derived from the Nimbus–7 ERB data, a comparison is made with the ERBE clear sky fluxes using zonal profiles. The analysis of ERBE data is done for the seasons of JJA 1985, SON 1985, DJF 1986 and MAM 1985. Figures 7–10 show zonally averaged profiles of the Nimbus–7 and ERBE derived clear sky SW, LW and net fluxes for each of the four seasons. Also shown on these figures as a histogram for the SW and LW fluxes is the zonal average of the number of observations below 20% cloudiness for each grid box. From these figures it can be seen that the SW fluxes compare reasonably well for most latitudes except poleward of about 45° for the JJA, SON, and DJF seasons. The largest discrepancy occurs during the DJF season south of 45° (Figure 9). This is due, primarily, to the cloud contamination of the Nimbus–7 fluxes by the persistent southern midlatitude clouds, as shown by the small number of clear sky observations. The differences in the polar regions are less important due to the difficulty in distinguishing between ice/snow and cloud for either data set. On a globally averaged basis the Nimbus–7 clear sky SW fluxes are about 3–4 Wm^{-2} higher than ERBE fluxes as seen in Table 2. Cloud contamination of the Nimbus–7 fluxes may explain the difference between the two data sets.

The behavior of the clear sky LW fluxes for Nimbus–7 and ERBE are very similiar except that the Nimbus–7 fluxes are consistently biased low. As expected, the globally averaged LW fluxes for Nimbus–7 and ERBE presented in Table 2 show the Nimbus–7 fluxes to be roughly 5–6 Wm^{-2} lower than those from ERBE. This bias of the Nimbus–7 LW fluxes is most likely due to cloud contamination. However, it cannot be ruled out that this discrepancy may be due, in part, to the high bias of ERBE clear sky fluxes noted earlier. The clear sky net fluxes compare very well except for perhaps south of 45° for the DJF and SON seasons. From Table 2 the globally averaged net fluxes for ERBE and Nimbus–7 exhibit about a 2–3 Wm^{-2} difference.
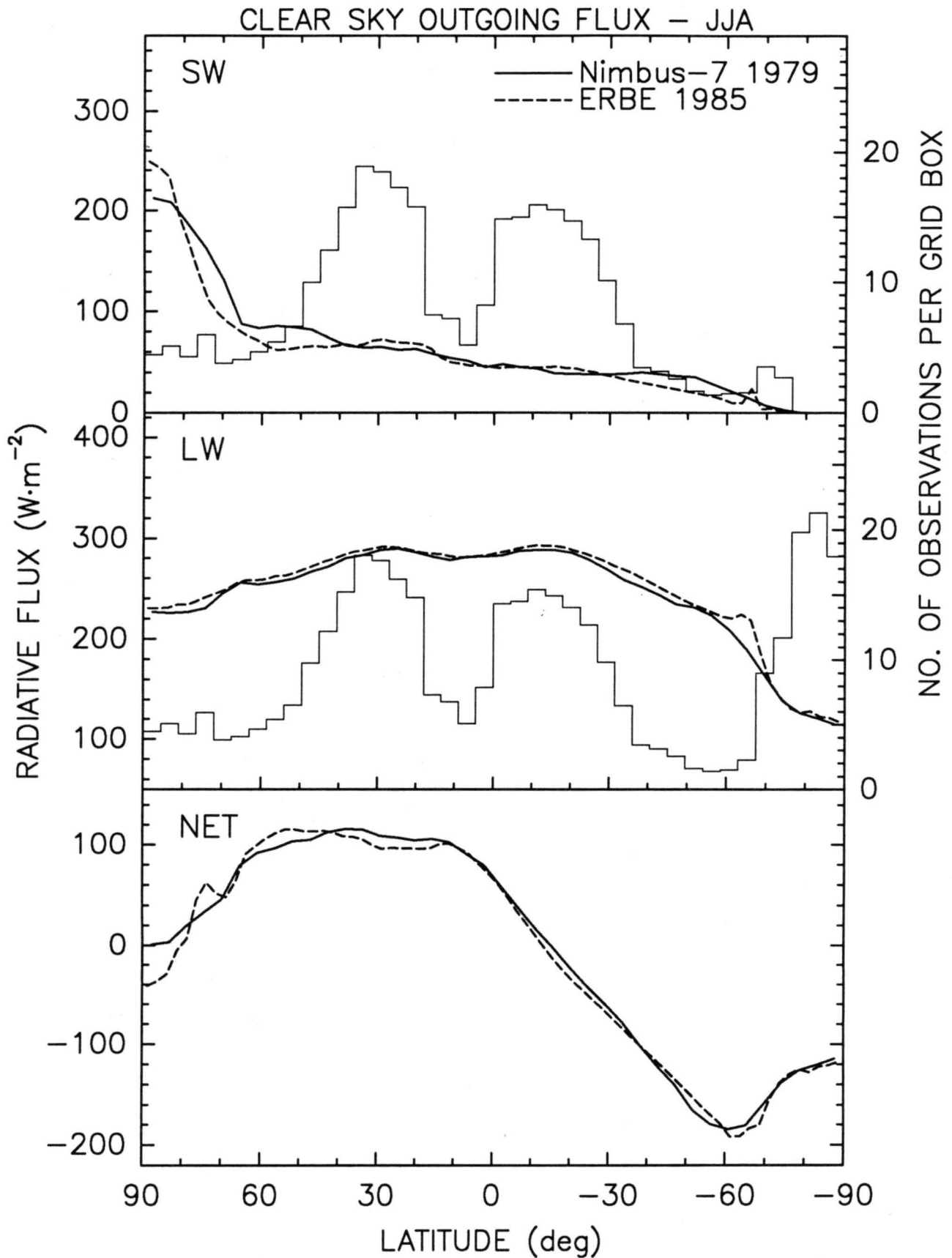
15

Figure 7. Zonally averaged clear sky reflected flux (SW), emitted flux (LW), and net flux (NET), in Wm^{-2}, as a function of latitude derived from Nimbus-7 (solid) and ERBE (dashed) data for the JJA season. Also included for the Nimbus-7 SW and LW fluxes is the zonal average of the number of observations below 20% cloudiness for each grid box.
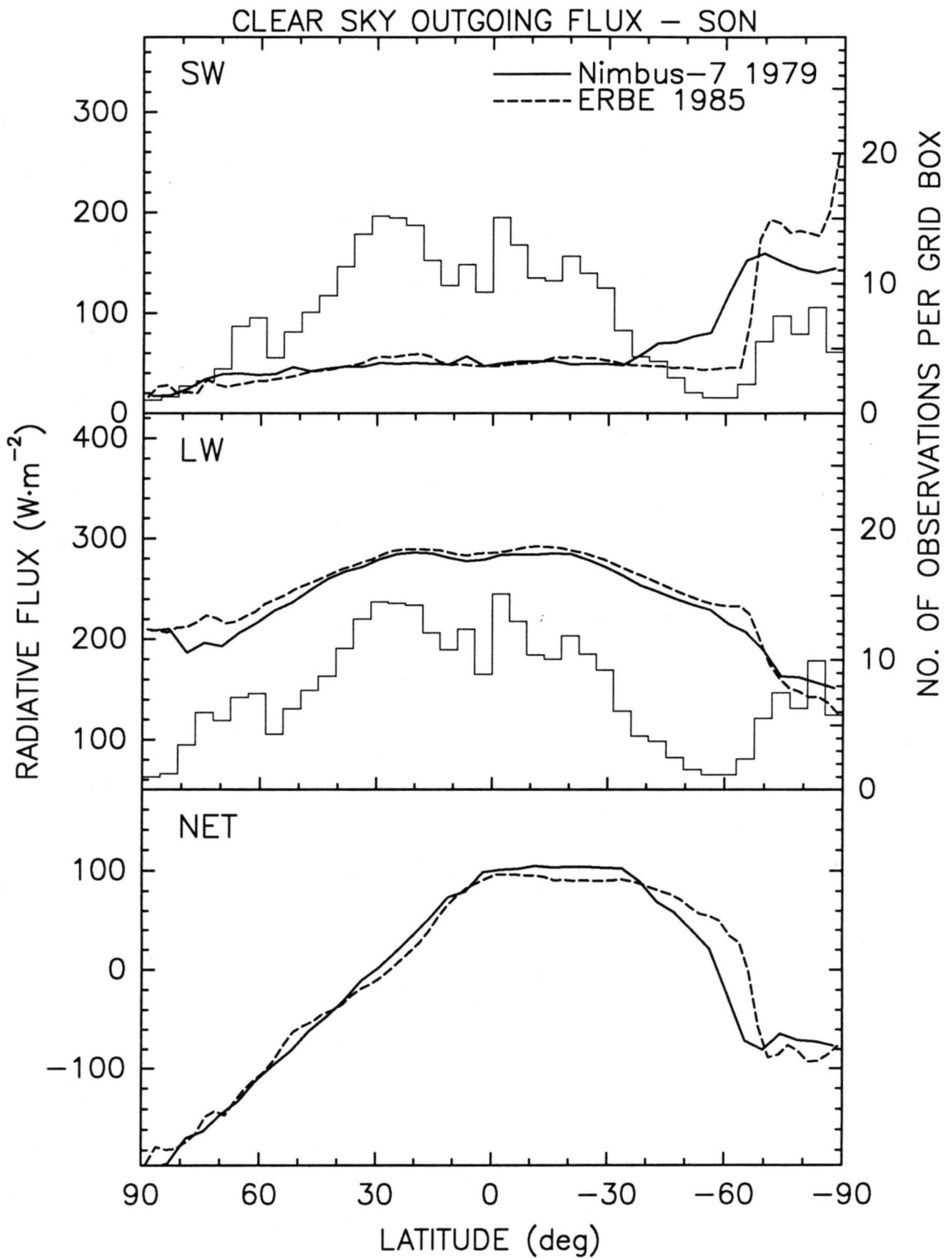
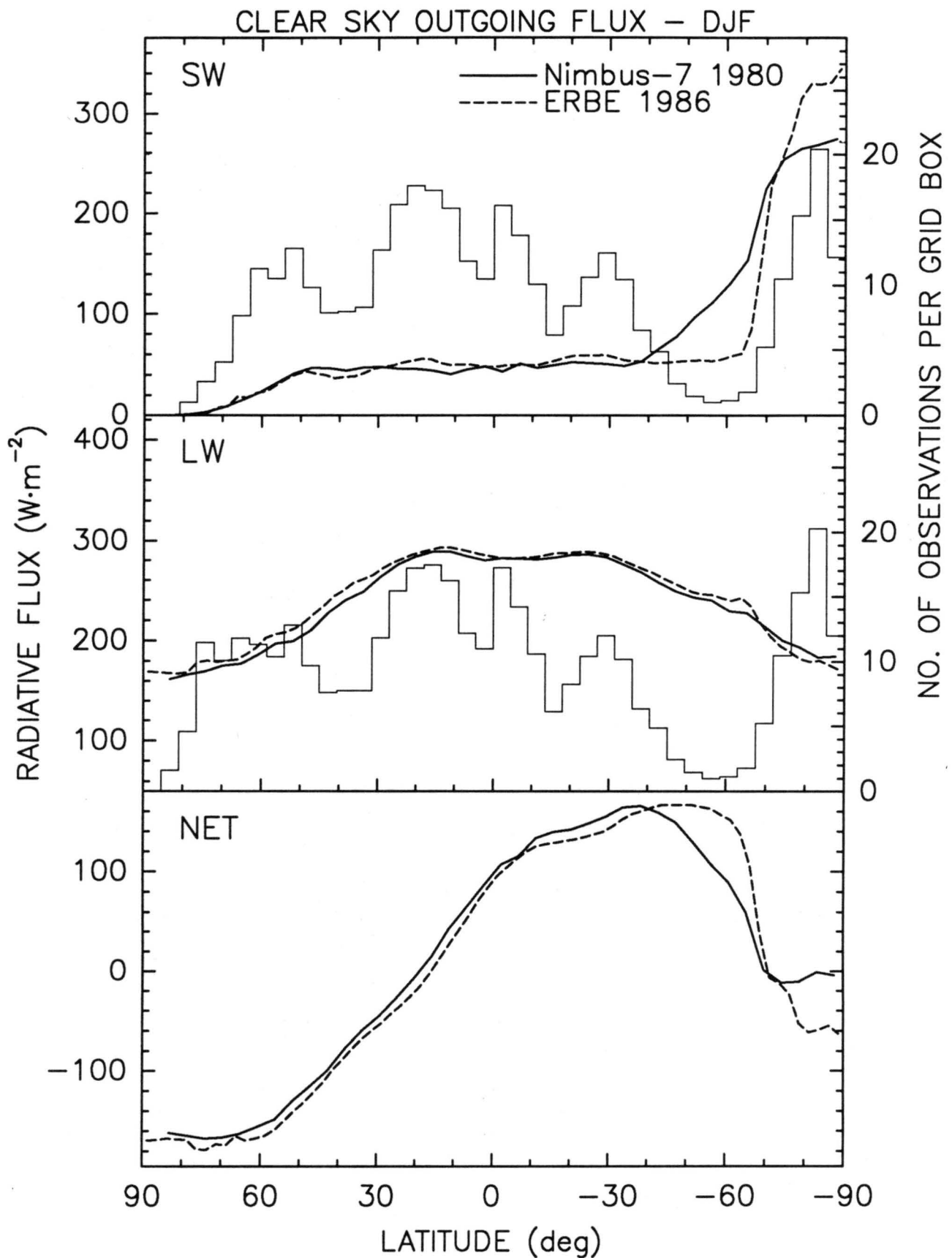Figure 8. Same as Fig. 7 except for the SON season.
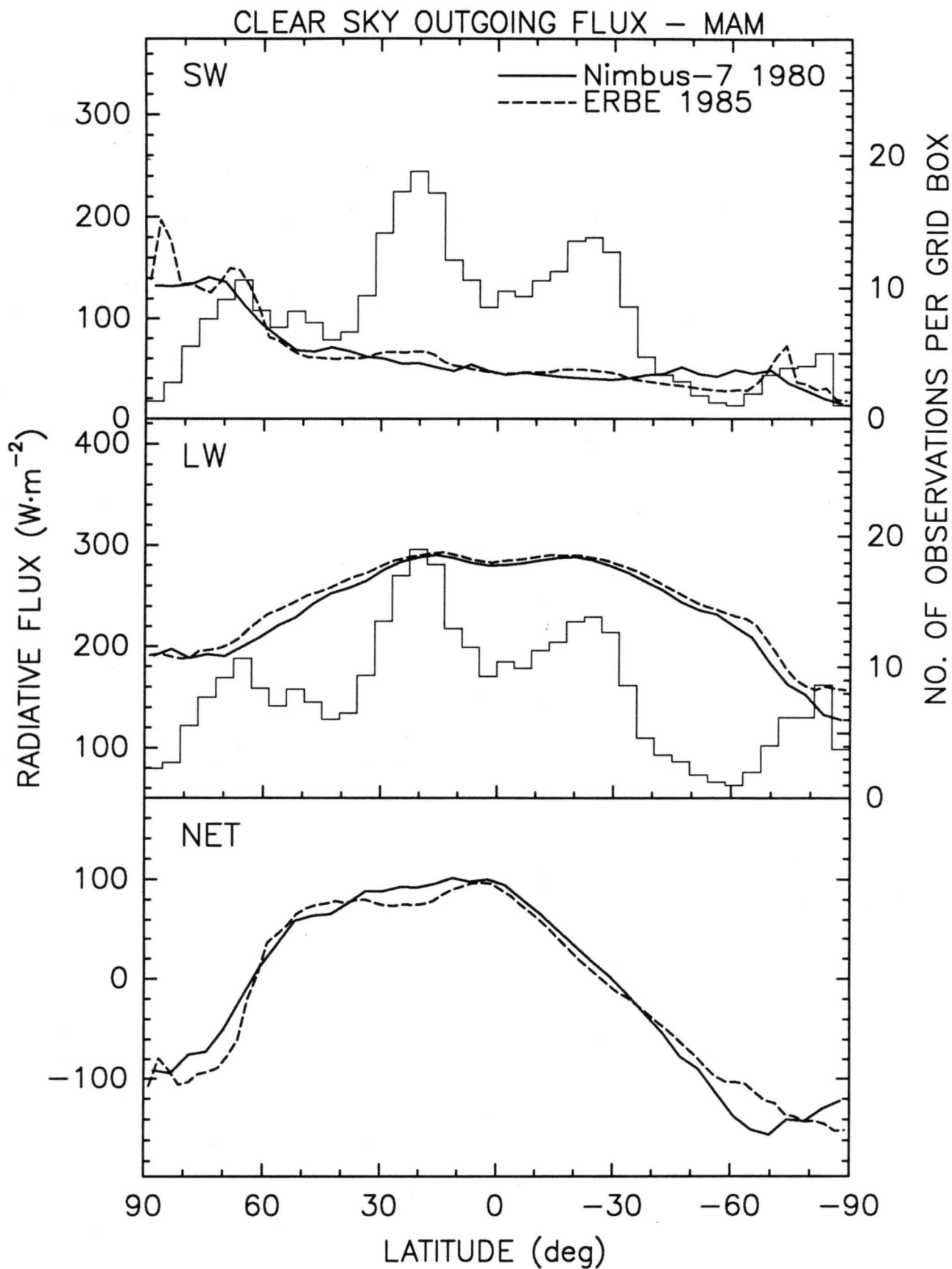
Figure 9. Same as Fig. 7 except for the DJF season.

CLEAR SKY OUTGOING FLUX – MAM

Figure 10. Same as Fig. 7 except for the MAM season.

Table 2: Globally averaged clear sky LW, SW and net fluxes (Wm^{-2}) derived from Nimbus-7 and ERBE (in parentheses) data.

Season	SW	LW	Net
JJA	54.1 (49.9)	263.4 (268.3)	15.4 (12.6)
SON	57.5 (53.3)	258.9 (265.6)	28.6 (28.4)
DJF	59.4 (55.5)	255.7 (260.8)	38.9 (35.0)
MAM	55.3 (56.1)	259.1 (265.2)	26.1 (23.3)
Annual	56.6 (53.7)	259.3 (265.0)	27.2 (24.8)

4. Cloud Effect Results

One way to describe the influence of clouds on the ERB is through the concept of cloud radiative forcing (see, e.g., Charlock and Ramanathan, 1985; Ramanathan, 1987). In this study, the term cloud radiative forcing will be referred to, hereafter, as cloud effect. It is defined specifically as the difference in the flux at the TOA when no clouds exist (the clear sky flux) and when clouds are present. Physically speaking, the cloud effect can be interpreted as the amount of radiative heating or cooling of the surface–atmosphere column due to the presence of clouds. This type of analysis has been used in several recent studies of the ERB (eg., Ramanathan, 1989a, 1989b; Harrison *et al.*, 1990) and can be used to obtain a quantitative estimate (in terms of radiative flux) of the direct effect of clouds on the ERB. The LW and SW cloud effects may be expressed, respectively, as:

$$C_{LW} = F_{clr} - F_{cldy} \tag{2}$$

and

$$C_{SW} = \frac{S_o}{4}(\alpha_{clr} - \alpha_{cldy}), \tag{3}$$

where F_{cldy} and α_{cldy} are the cloudy sky (or total) LW flux and SW albedo, respectively. The net effect of clouds on the ERB can be obtained from:

$$C_{net} = C_{LW} + C_{SW}. \tag{4}$$

The clear sky albedos and LW fluxes are those derived from the previous section and the cloudy sky albedos and LW fluxes follow directly from the Nimbus–7 ERB observations.
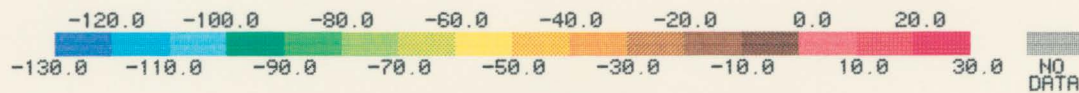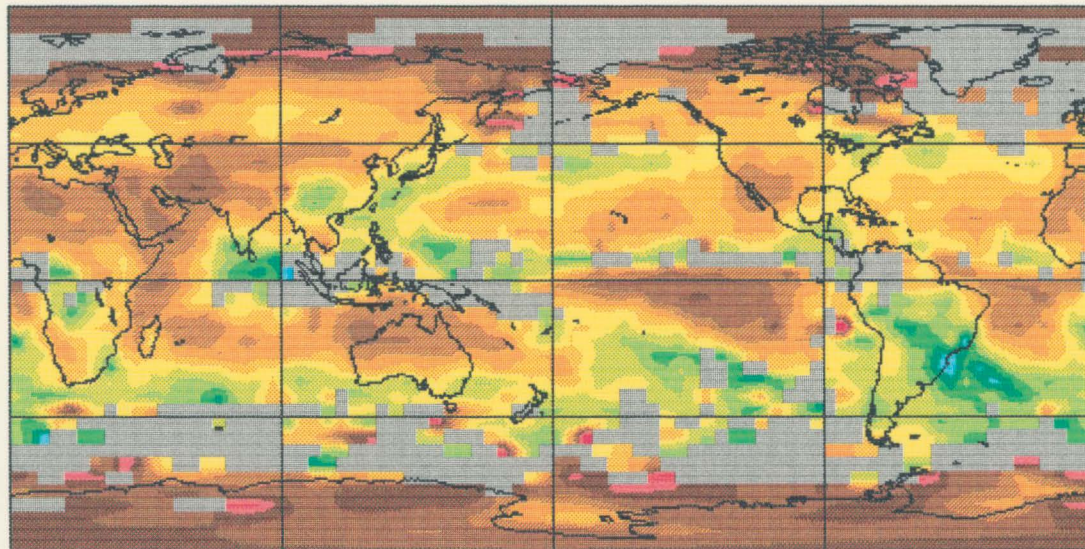
The global distribution of C_{SW} (Wm^{-2}) for the four seasons is shown in Figures 11 and 12. What can be concluded from these figures is that, quite expectedly, clouds produce a negative SW effect because they reflect a large portion of the incoming solar energy back into space. The strongest and most extensive regions of this negative effect occur not in the tropics as one might expect, but in areas of midlatitude storm tracks and stratus decks. This effect is greatest during the southern hemisphere summer season (see Figure 12a) and can surpass $-130\ Wm^{-2}$. Most areas

21

a

-120.0   -100.0   -80.0   -60.0   -40.0   -20.0   0.0   20.0
-130.0   -110.0   -90.0   -70.0   -50.0   -30.0   -10.0   10.0   30.0   NO DATA

SW CLOUD EFFECT (W/M**2)
JJA 1979

b

-120.0   -100.0   -80.0   -60.0   -40.0   -20.0   0.0   20.0
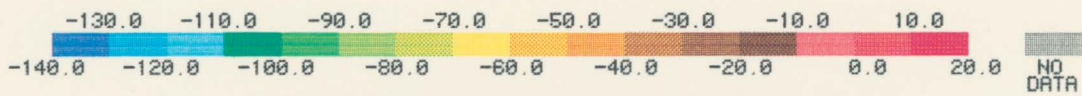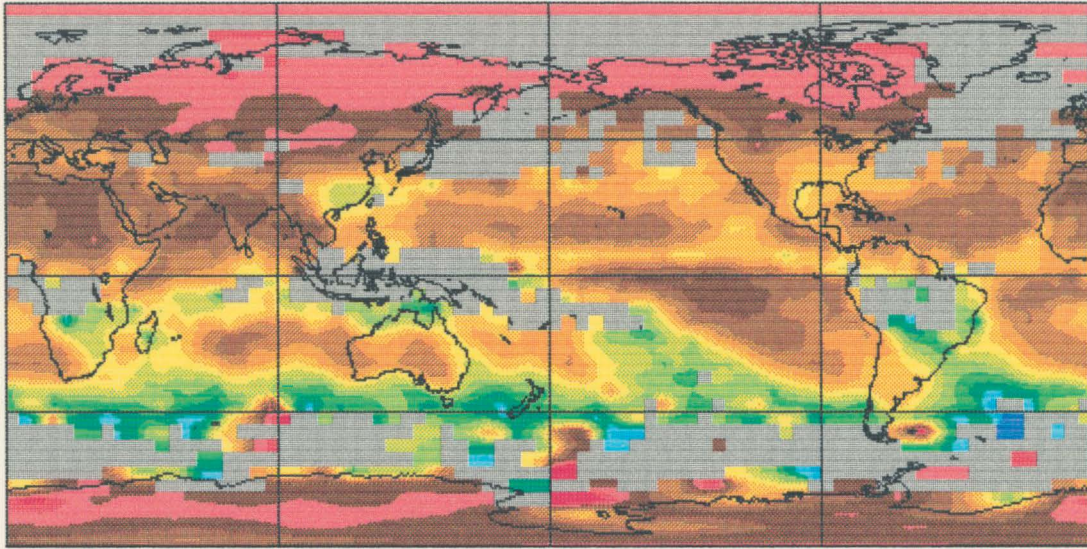-130.0   -110.0   -90.0   -70.0   -50.0   -30.0   -10.0   10.0   30.0   NO DATA
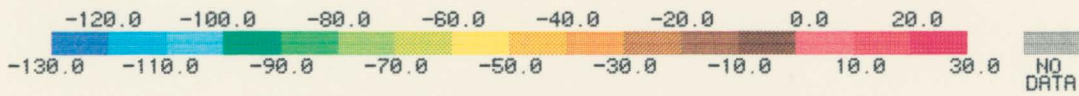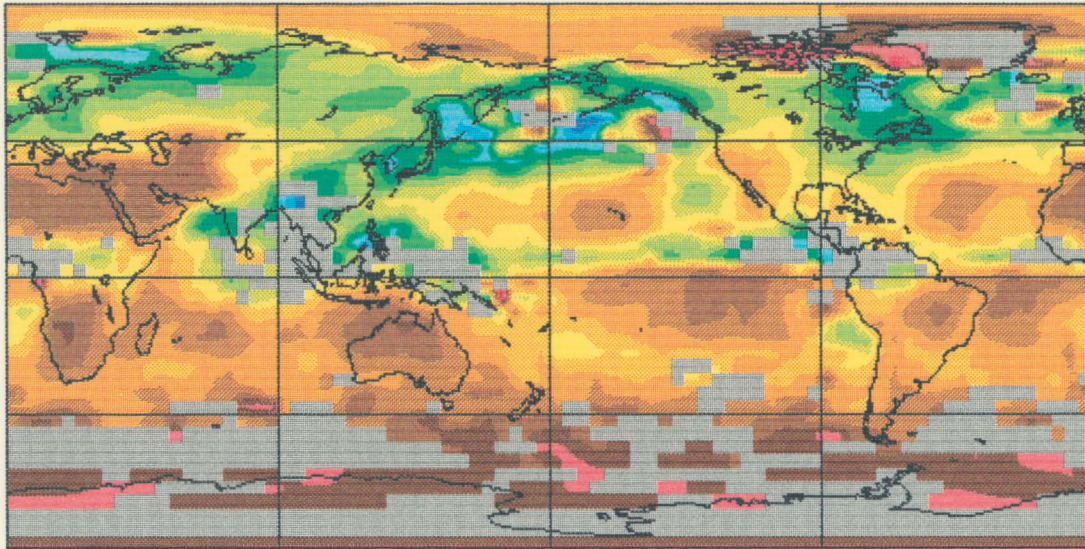
SW CLOUD EFFECT (W/M**2)
SON 1979

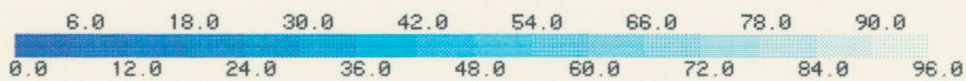Figure 11. Global distributions of C_{SW} (Wm^{-2}) for (a) JJA 1979 and (b) SON 1979.

a

-130.0   -110.0   -90.0   -70.0   -50.0   -30.0   -10.0   10.0
-140.0   -120.0   -100.0   -80.0   -60.0   -40.0   -20.0   0.0   20.0   NO DATA

SW CLOUD EFFECT (W/M**2)
DJF 1980

b

-130.0   -110.0   -90.0   -70.0   -50.0   -30.0   -10.0   10.0
-140.0   -120.0   -100.0   -80.0   -60.0   -40.0   -20.0   0.0   20.0   NO DATA
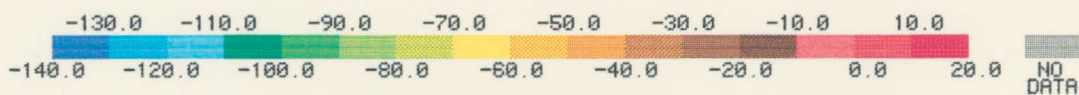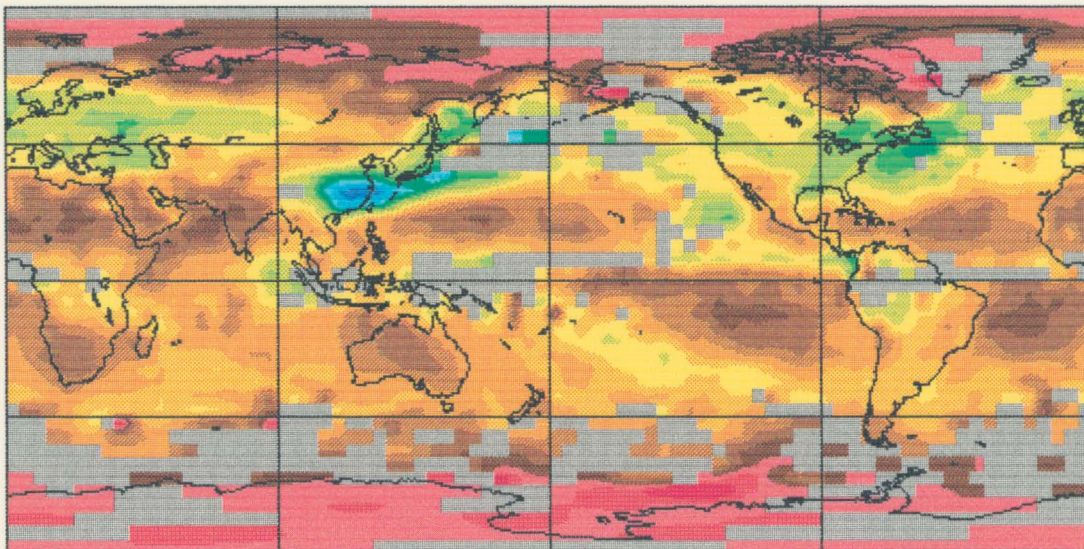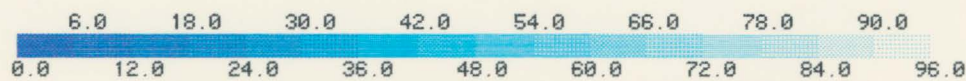
SW CLOUD EFFECT (W/M**2)
MAM 1980

Figure 12. Same as Fig. 11 except for (a) DJF 1980 and (b) MAM 1980.
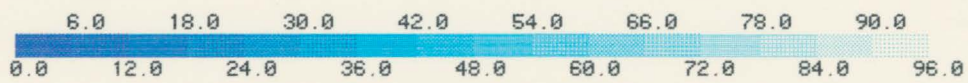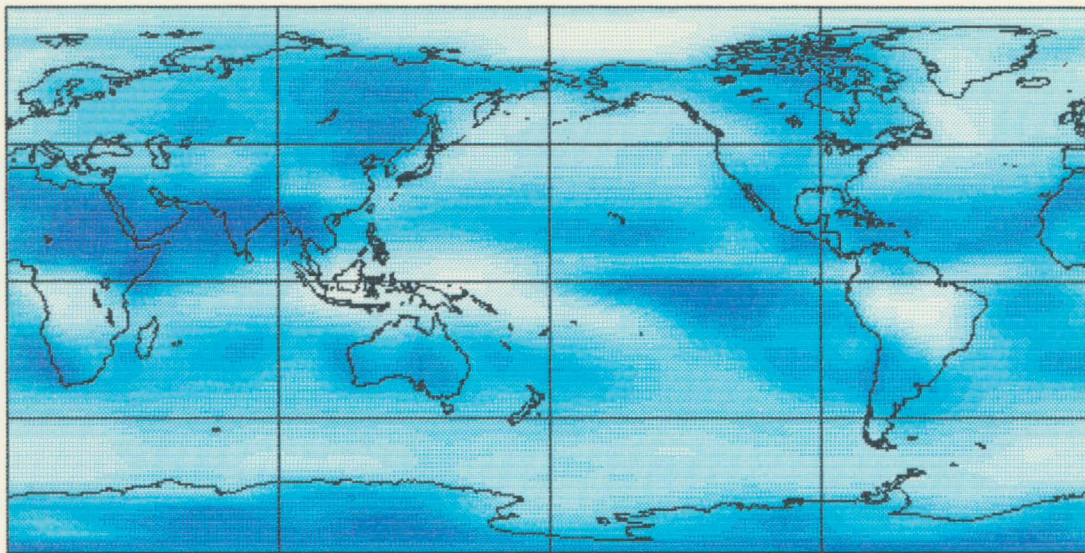
a
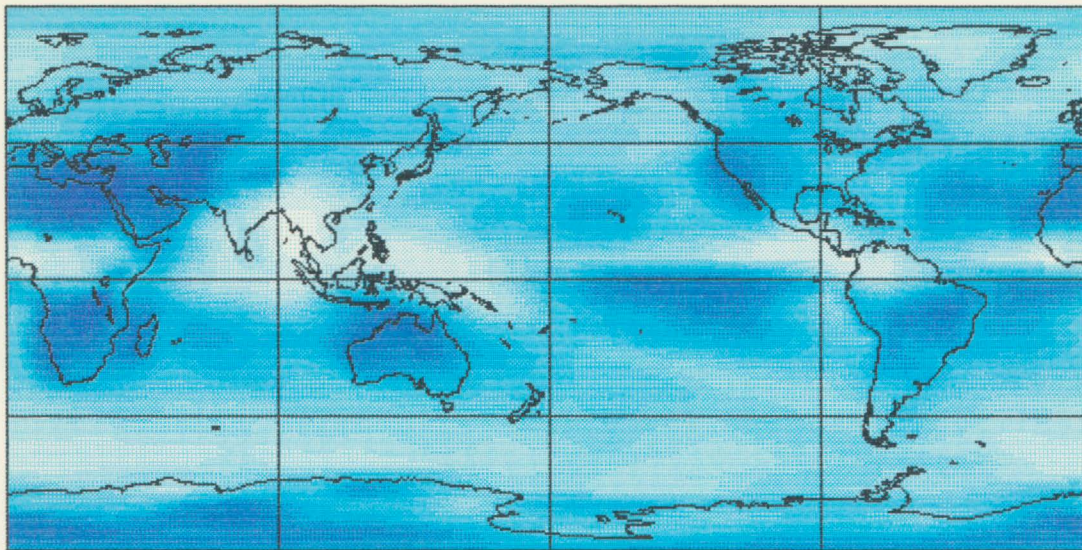
TOTAL CLOUD AMOUNT (%)
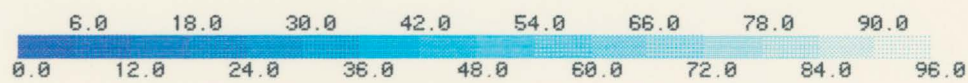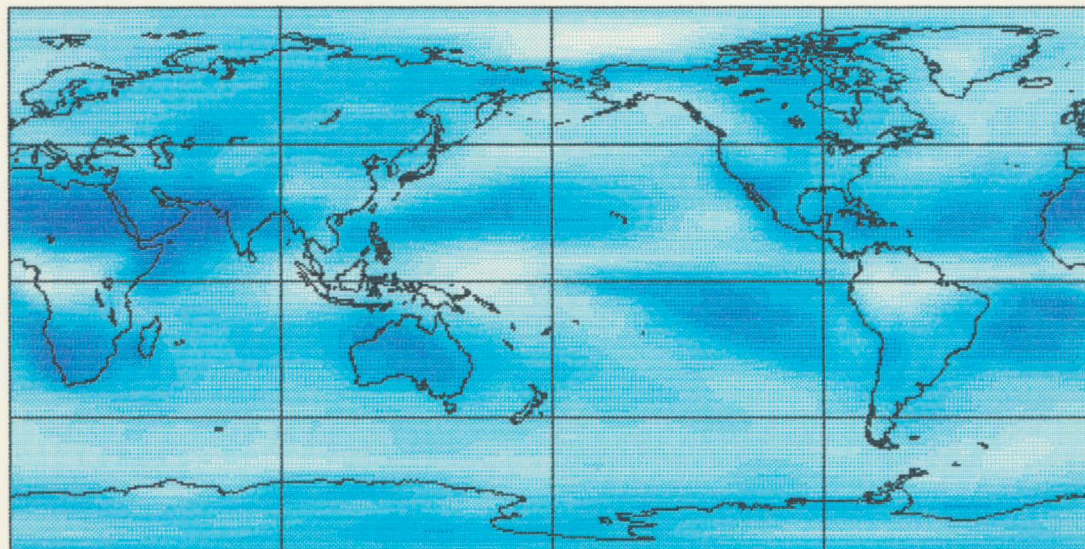JJA 1979

b
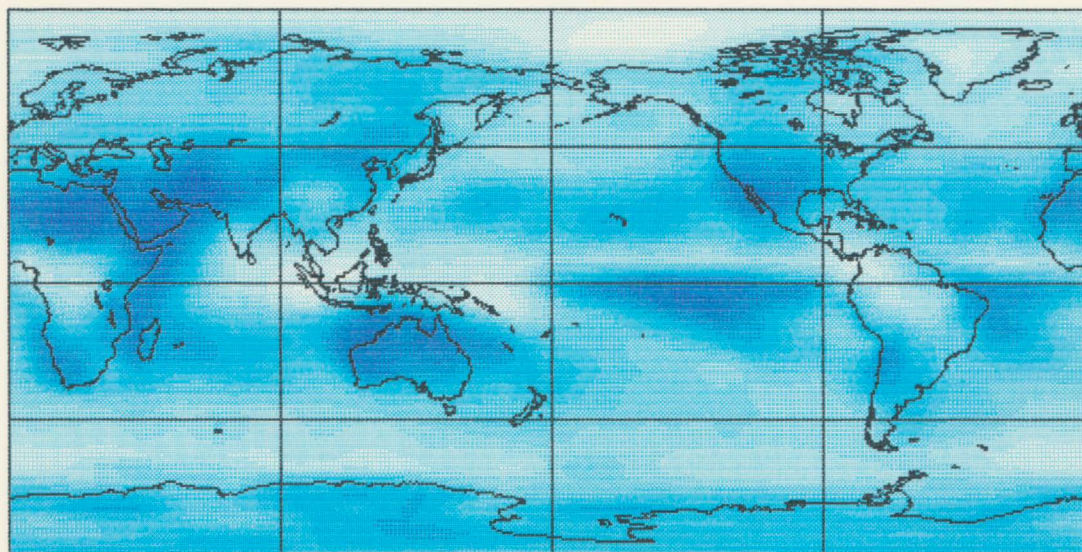
TOTAL CLOUD AMOUNT (%)
SON 1979

Figure 13. Global distributions of Nimbus–7 THIRS/TOMS derived total cloud amount (%) for (a) JJA 1979 and (b) SON 1979.

a

TOTAL CLOUD AMOUNT (%)
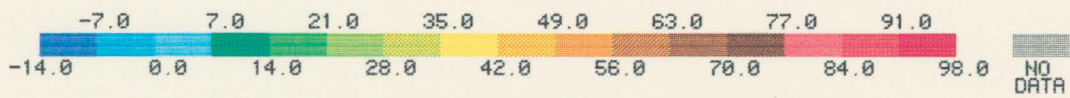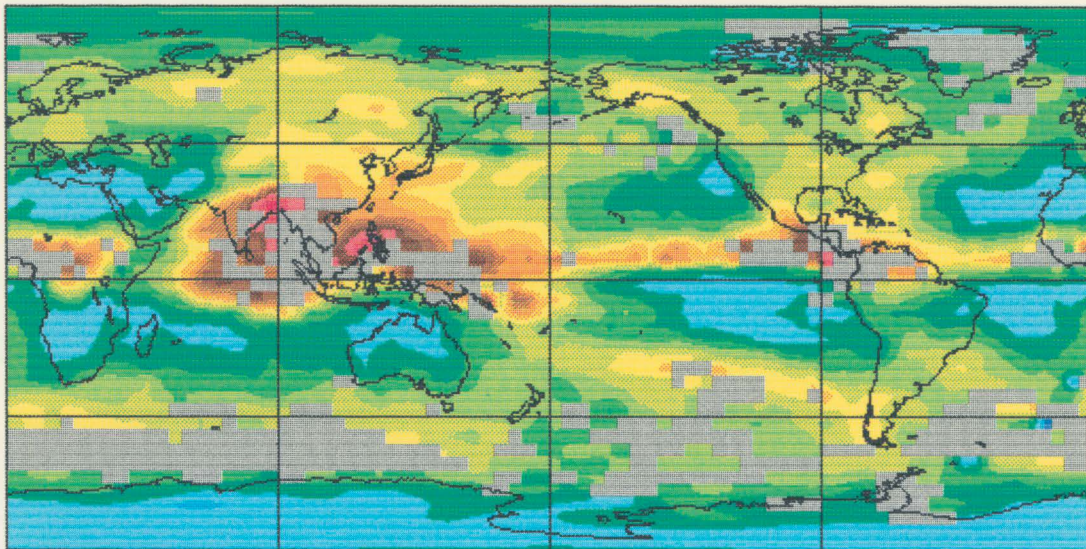DJF 1980

b

TOTAL CLOUD AMOUNT (%)
MAM 1980

Figure 14. Same as Fig. 13 except for (a) DJF 1980 and (b) MAM 1980.

25

near the polar regions show a small positive shortwave cloud effect. Because of the difficulties in obtaining clear sky albedos where bright snow and ice exists, it is uncertain whether this positive cloud effect is real, an artifact of the minimum albedo method or, possibly, a result of inaccuracies in the cloudiness data set.

If one compares the Nimbus-7 total cloud amount global maps in Figures 13 and 14 with the corresponding SW cloud effect maps it can be seen that regions of abundant cloudiness correspond well with large negative effects, while areas with less cloudiness are associated with a small cloud effect. Although there is, naturally, a correlation between cloudiness and negative SW cloud effect, areas of the most extreme cloudiness do not necessarily produce the strongest effect. For instance, a comparison of Figures 11a and 13a for the JJA season reveals that the areas of greatest cloudiness, which occur along the ITCZ and in the Asian monsoon regions, are associated with a SW cloud effect that is comparable to or slightly smaller than the regions of the northern Pacific ocean where the cloudiness is less. This may be a consequence of the seasonal average solar zenith angle for the northern midlatitudes being somewhat larger than the tropics, resulting in higher cloud albedos and thus a larger SW effect.
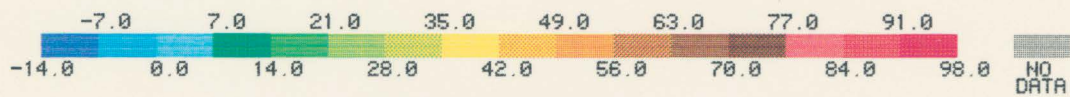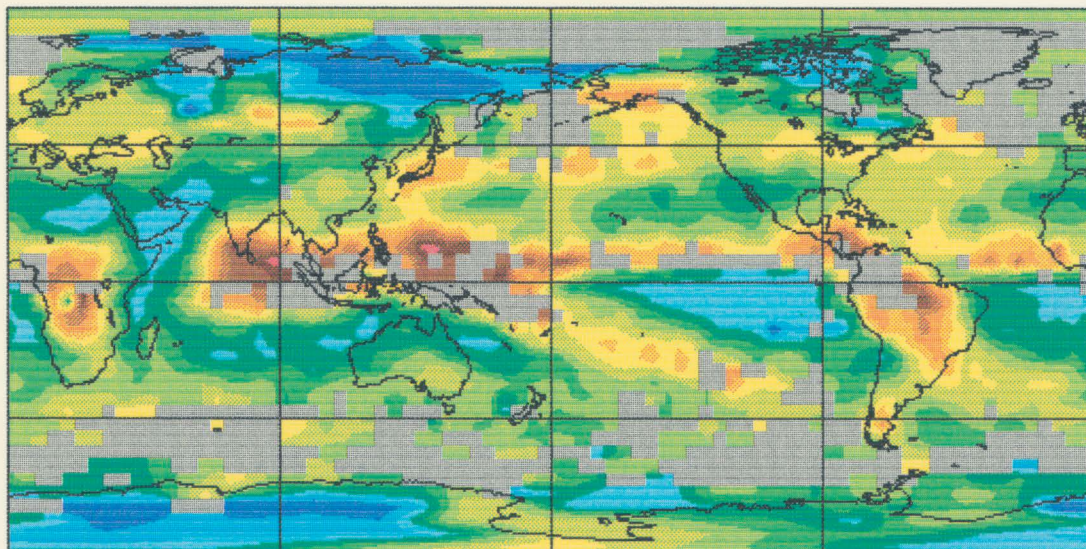
In Figures 15 and 16 the global maps of C_{LW} (Wm^{-2}) for the four seasons are shown. The cloud effect in the LW spectrum is generally positive. With the introduction of clouds LW radiation is emitted to space from the cold cloud tops, thereby producing less emission than with a cloud-free atmosphere. The LW cloud effect is greatest in the tropics where it can exceed 90 Wm^{-2} in the northern hemisphere summer (see Figure 15a). This effect is caused by strong convection that produces very high and optically thick clouds that emit less LW radiation to space, hence increasing the LW effect. The LW effect is smallest near the poles and in regions of persistent subtropical high pressure systems. In areas of marine stratocumulus clouds the LW effect is also small. These low lying clouds emit, from cloud top, at a temperature nearly that of the sea surface temperature. Regions of negative LW effect can appear in high latitudes, particularly during the spring or fall (see Figures 15b and 16b), due to the low-level temperature inversion that causes the clouds to emit at a temperature greater than the surface temperature.

a

-7.0   7.0   21.0   35.0   49.0   63.0   77.0   91.0
-14.0   0.0   14.0   28.0   42.0   56.0   70.0   84.0   98.0   NO DATA

LW CLOUD EFFECT (W/M**2)
JJA 1979

b

-7.0   7.0   21.0   35.0   49.0   63.0   77.0   91.0
-14.0   0.0   14.0   28.0   42.0   56.0   70.0   84.0   98.0   NO DATA
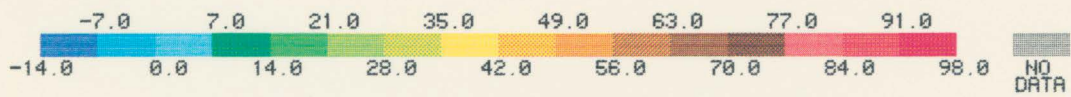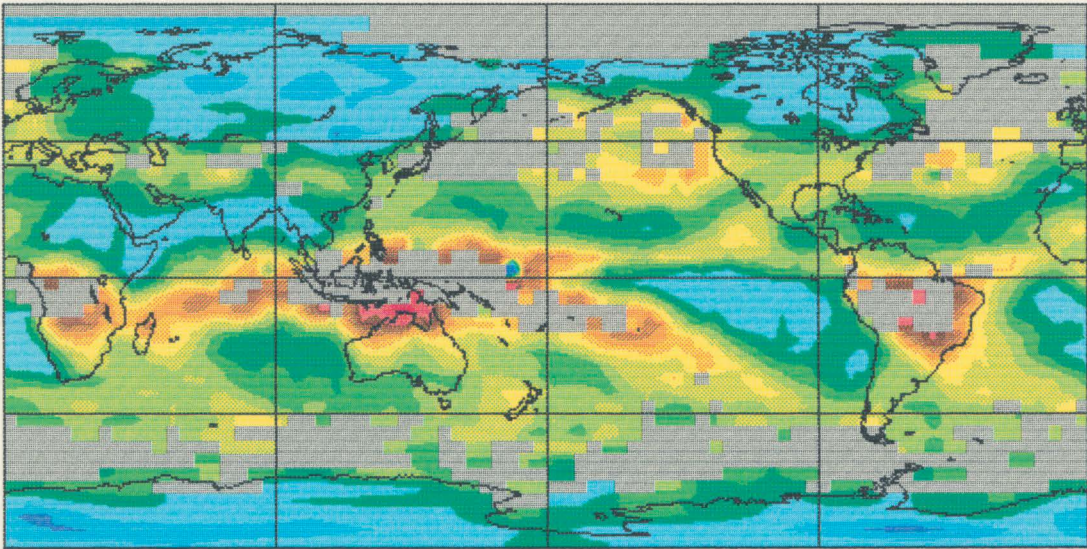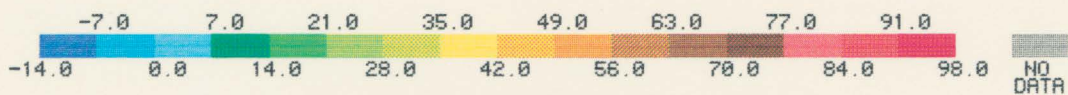
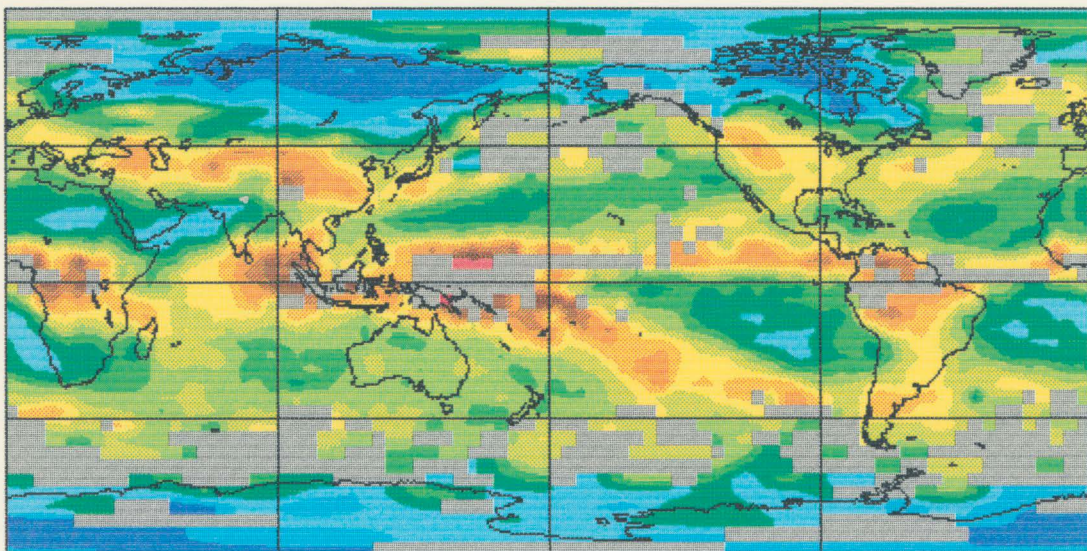LW CLOUD EFFECT (W/M**2)
SON 1979

Figure 15. Global distributions of C_{LW} (Wm^{-2}) for (a) JJA 1979 and (b) SON 1979.
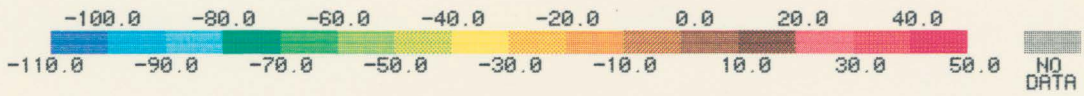
27

a

LW CLOUD EFFECT (W/M**2)
DJF 1980

b

LW CLOUD EFFECT (W/M**2)
MAM 1980

Figure 16. Same as Fig. 15 except for (a) DJF 1980 and (b) MAM 1980.

a

-100.0   -80.0   -60.0   -40.0   -20.0   0.0   20.0   40.0

-110.0   -90.0   -70.0   -50.0   -30.0   -10.0   10.0   30.0   50.0   NO DATA

NET CLOUD EFFECT (W/M**2)
JJA 1979

b

-100.0   -80.0   -60.0   -40.0   -20.0   0.0   20.0   40.0

-110.0   -90.0   -70.0   -50.0   -30.0   -10.0   10.0   30.0   50.0   NO DATA

NET CLOUD EFFECT (W/M**2)
SON 1979

Figure 17. Global distributions of C_{net} (Wm^{-2}) for (a) JJA 1979 and (b) SON 1979.

a

NET CLOUD EFFECT (W/M**2)
DJF 1980
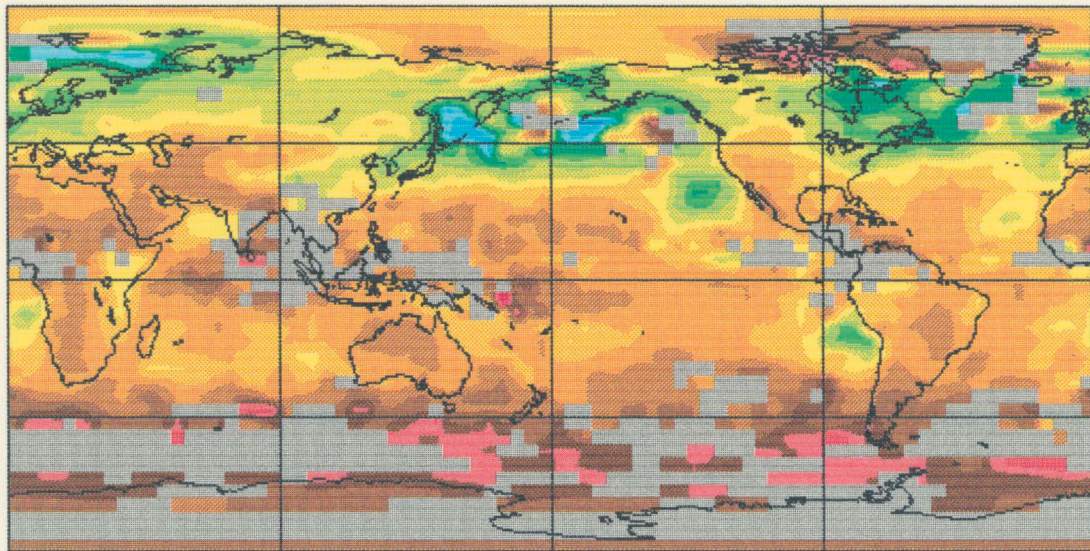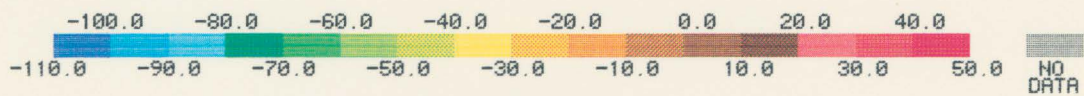
b

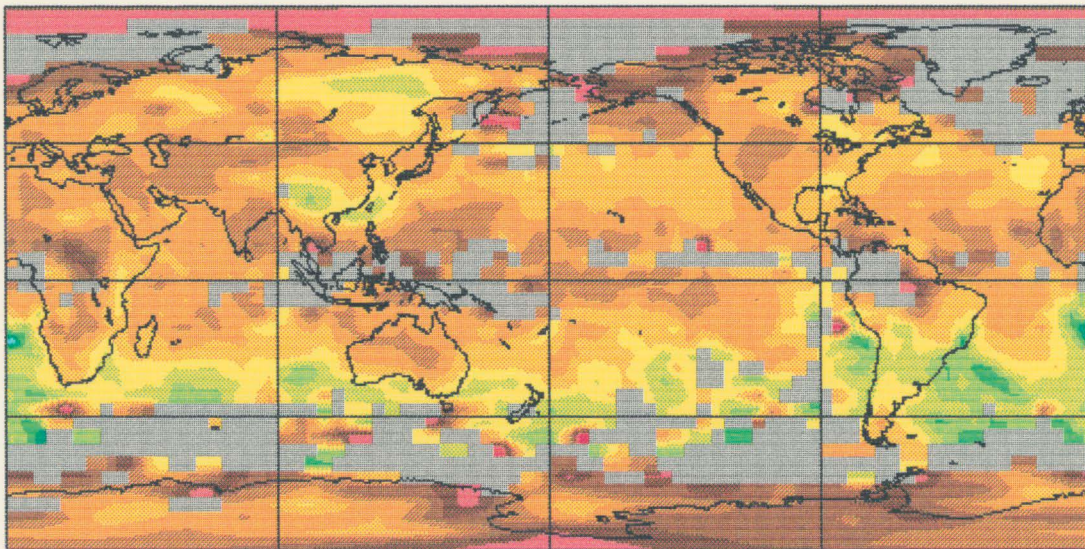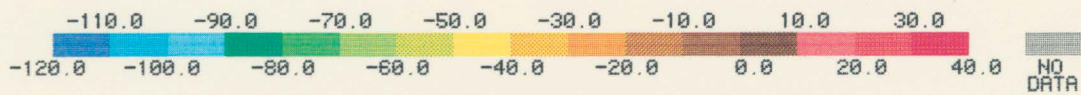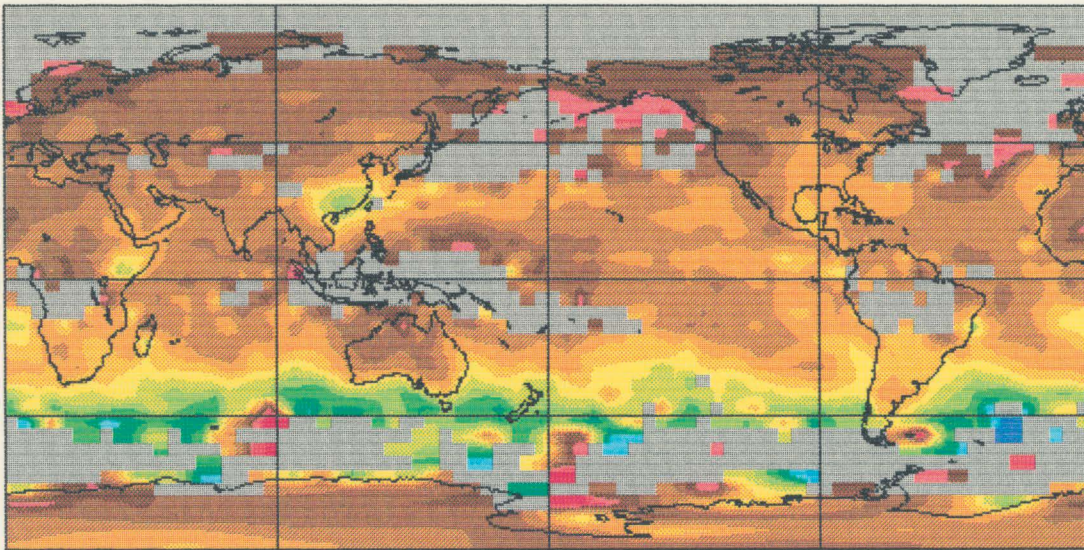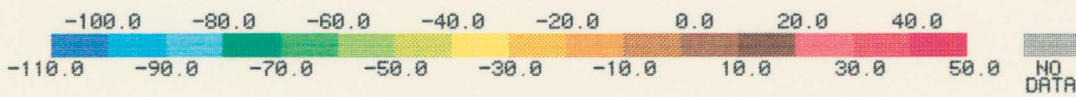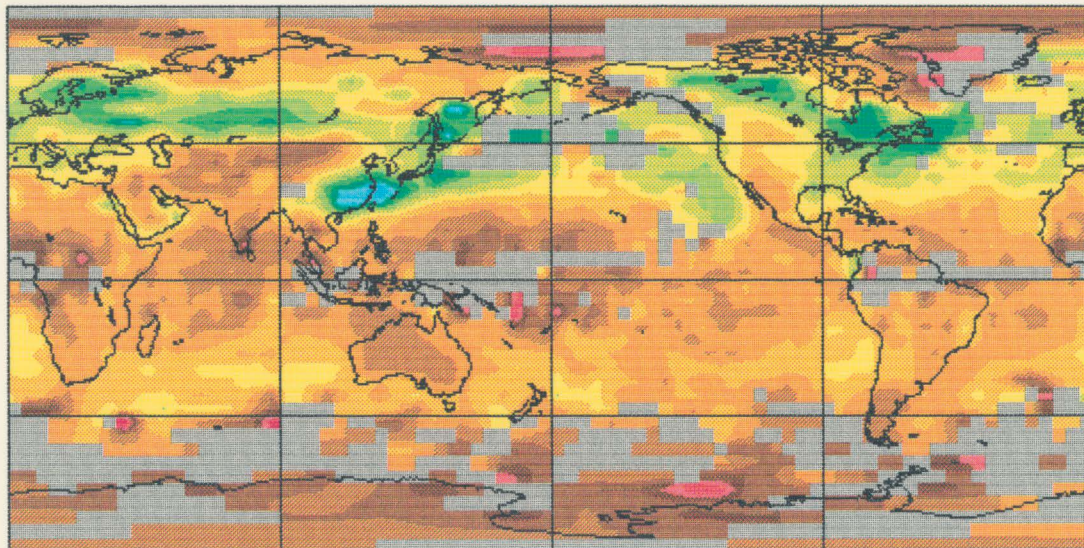

NET CLOUD EFFECT (W/M**2)
MAM 1980

Figure 18. Same as Fig. 17 except for (a) DJF 1980 and (b) MAM 1980.

The net effect C_{net} (Wm^{-2}) of the LW and SW cloud effects for the four seasons is shown in Figures 17 and 18. Over most of the globe the net cloud effect is negative with the greatest effect occurring in midlatitude summer regions (northern midlatudes for JJA 1979 and MAM 1980 and southern midlatitudes for DJF 1980). In addition there are large negative net cloud effects in areas of stratocumulus clouds. In the tropics there is a near cancellation of the LW and SW cloud effects resulting in a small negative net effect. This phenomenon has been observed in other ERB studies (eg. Ramanathan *et al.*, 1989a) and illustrates the reciprocal nature of the cloud albedo and outgoing LW flux in this region. Nearly all areas of positive net cloud effect occur in the polar regions where the determination of the cloud effect is uncertain.

Qualitative comparisons of the seasonal cloud effects obtained from the present study can be made with the cloud effects determined from ERBE using zonal averages. Figures 19–22 show the zonally averaged SW, LW, and net cloud effects for the JJA, SON, DJF, and MAM seasons, respectively. What is most characteristic of C_{SW} is the significant minimum that occurs when the northern midlatitudes (Figure 19) or southern midlatitudes (Figures 20 and 21) are illuminated by the sun. In addition, the ITCZ appears as a distinct minimum in the tropics, at least for the seasons of JJA and SON. The Nimbus–7 and ERBE data sets compare well except for regions poleward of about 45°. The large discrepancy seen for DJF in Figure 21 in the southern midlatitudes is most likely a consequence of cloud contamination of the Nimbus–7 clear sky fluxes. There are also differences between the two data sets in the polar regions; however, the SW cloud effects in these areas are uncertain for both data sets. On a globally averaged basis the Nimbus–7 values of C_{SW} are about 5 Wm^{-2} smaller than ERBE (see Table 3), resulting from cloud contamination of the clear sky SW fluxes discussed earlier.

The general latitudinal behavior of C_{LW} is represented as maxima in the tropics and midlatitudes with minima in the subtropical regions. The zonal profiles of C_{LW} obtained from Nimbus–7 data are, for the most part, biased with respect to the ERBE data at nearly all latitudes. This bias is revealed in the globally averaged values of C_{LW} in Table 3, where the Nimbus–7 values are
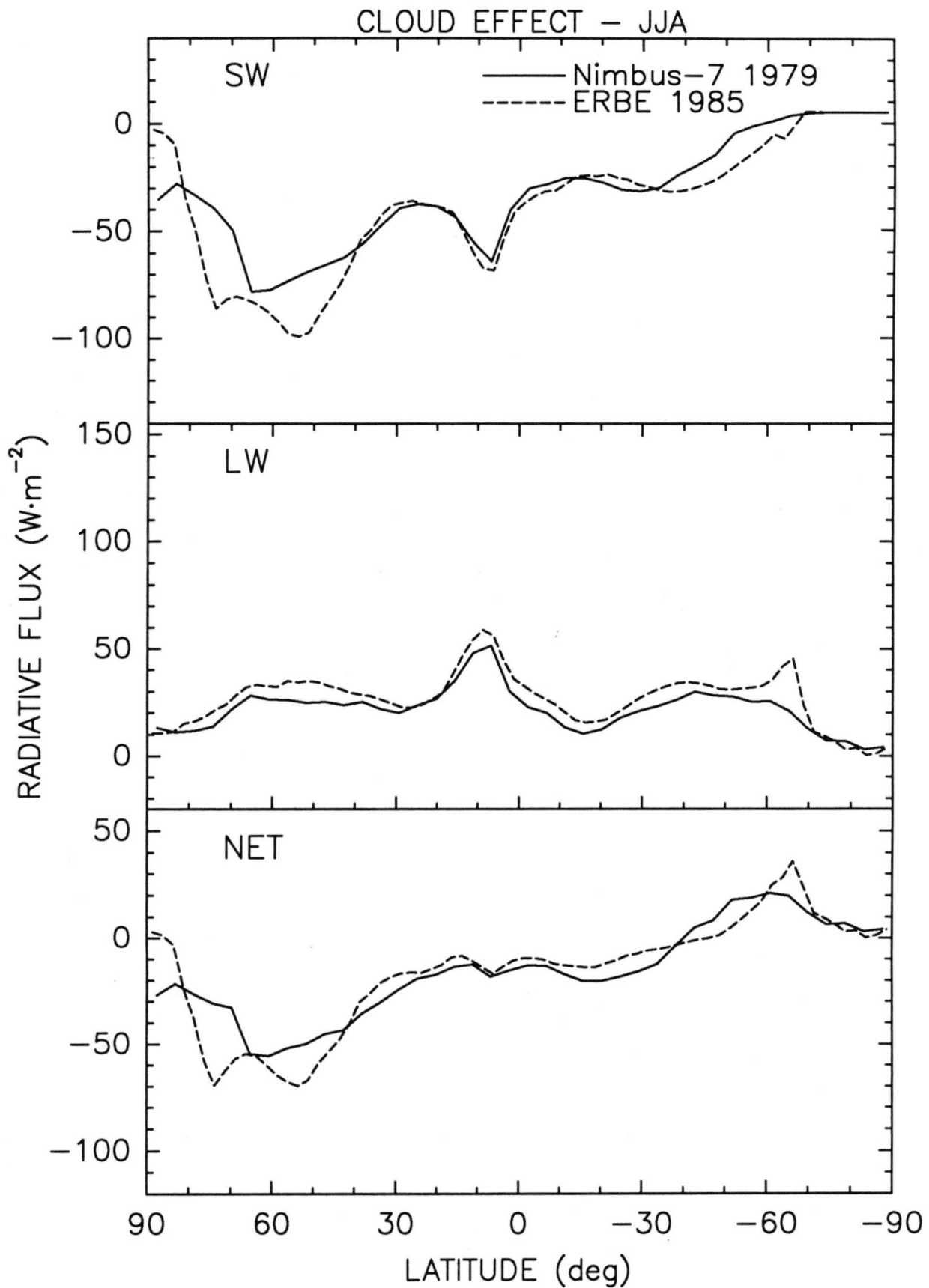
31

Figure 19. Zonally averaged quantities of C_{SW}, C_{LW}, and C_{net}, in Wm^{-2}, as a function of latitude derived from Nimbus-7 (solid) and ERBE (dashed) data for the JJA season.
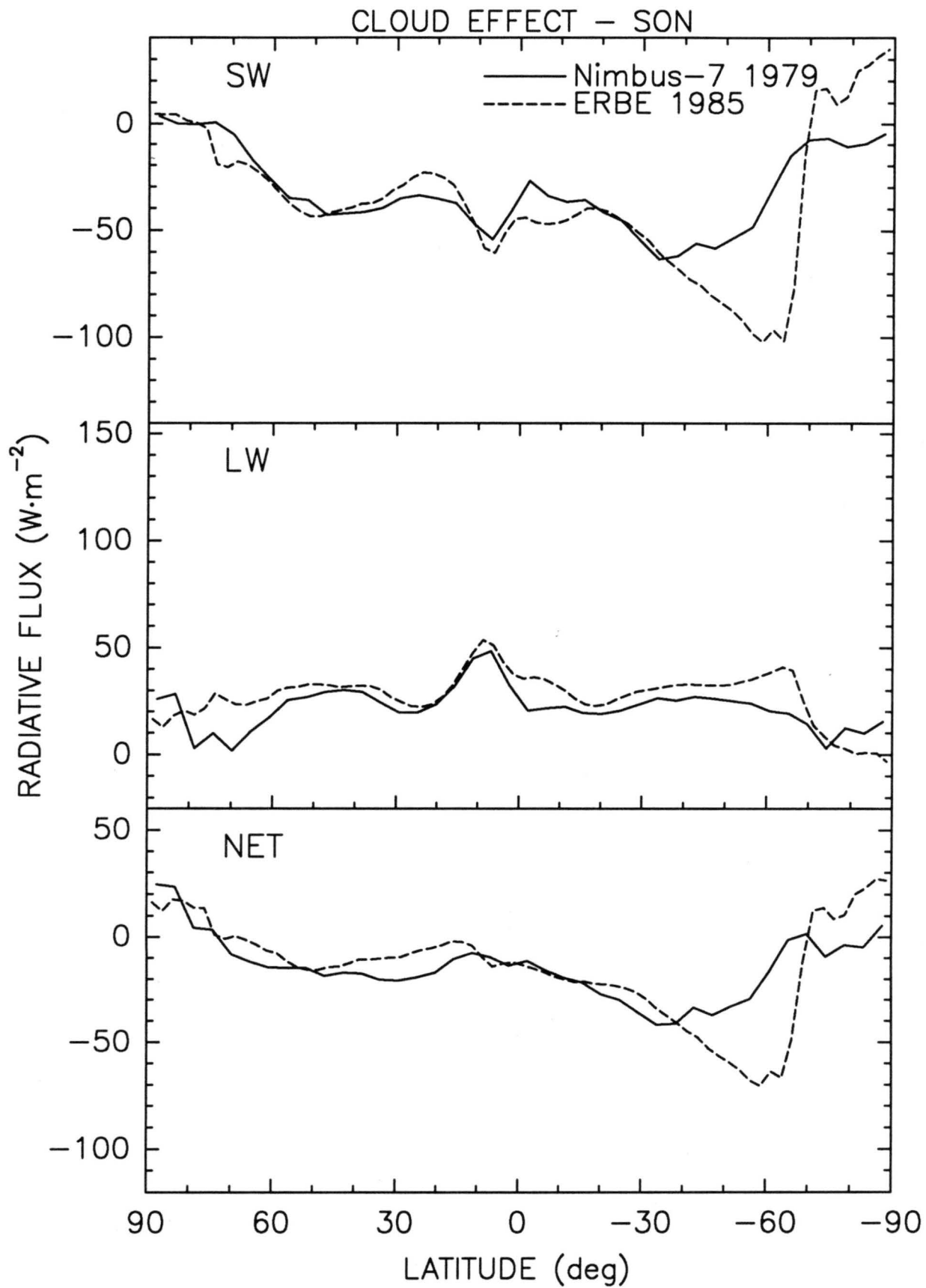
Figure 20. Same as Fig. 19 except for the SON season.
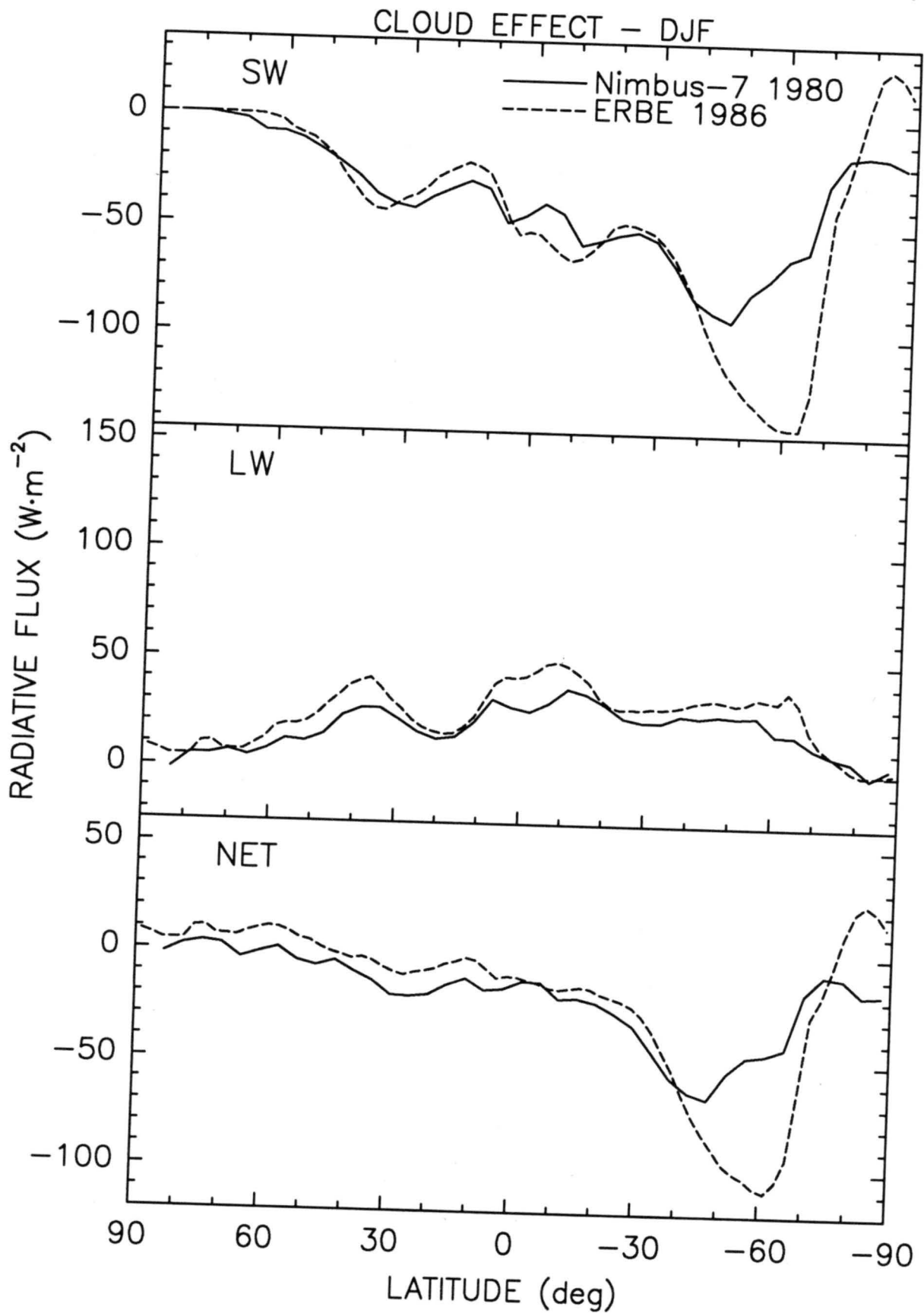
Figure 21. Same as Fig. 19 except for the DJF season.
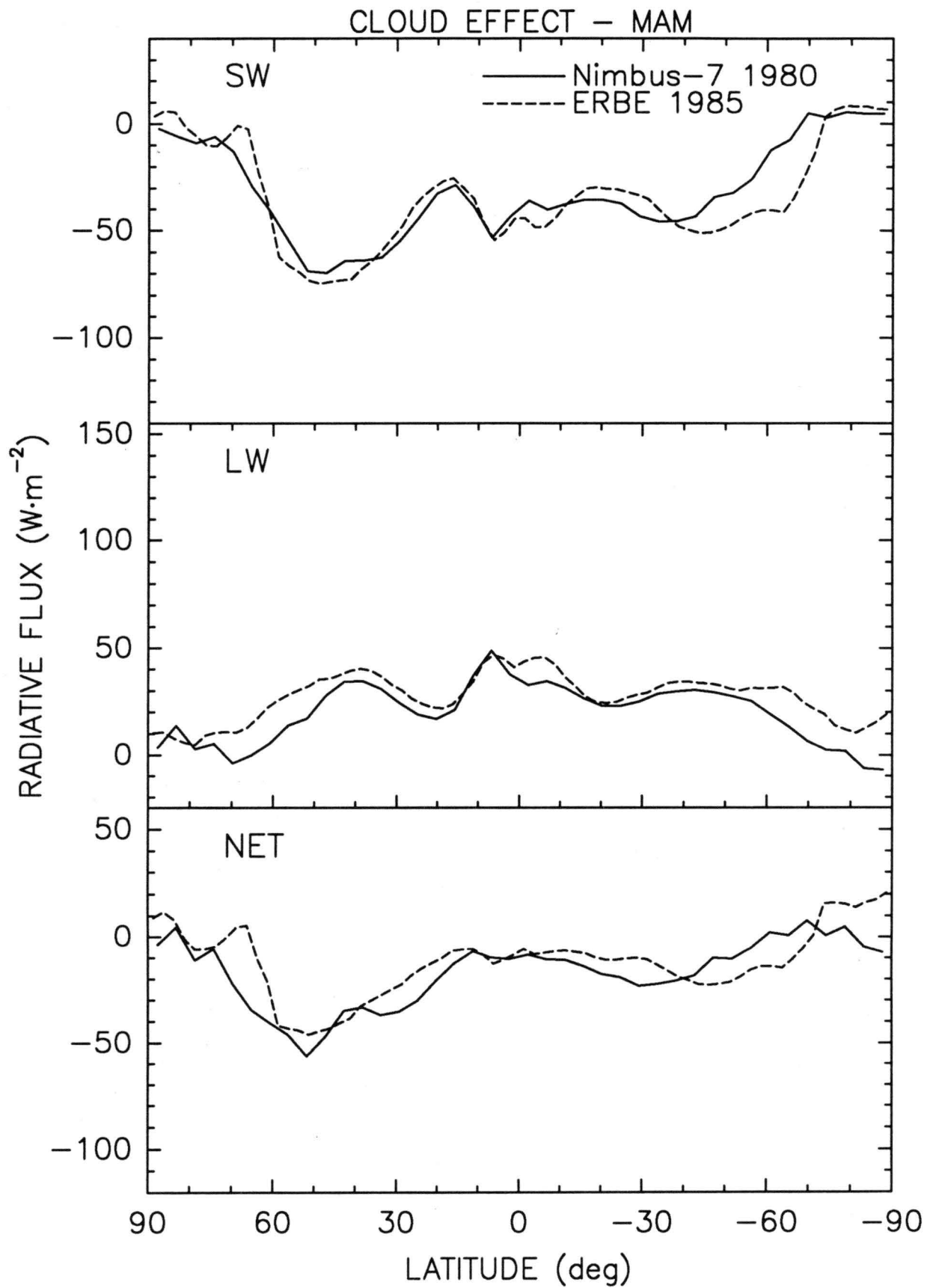
Figure 22. Same as Fig. 19 except for the MAM season.

Table 3: Globally averaged quantities of C_{LW}, C_{SW} and C_{net} (Wm^{-2}) derived from Nimbus-7 and ERBE (in parentheses) data.

Season	C_{SW}	C_{LW}	C_{net}
JJA	−42.1 (−46.6)	24.4 (30.0)	−17.7 (−16.4)
SON	−44.0 (−50.0)	24.5 (31.0)	−19.5 (−19.3)
DJF	−44.5 (−51.1)	22.2 (29.6)	−22.2 (−21.4)
MAM	−44.7 (−46.6)	25.2 (31.3)	−19.5 (−15.3)
Annual	−43.8 (−48.6)	24.1 (30.5)	−19.7 (−18.1)

about 6 Wm^{-2} lower than ERBE values and are consistent with cloud contamination of the clear sky LW fluxes.

The net cloud effect remains, for the most part, constant in the tropics from season to season for both Nimbus–7 and ERBE data, ranging from about –5 to –20 Wm^{-2}. The greatest seasonal changes in C_{net} from summer to winter occur in the midlatitudes, sometimes reaching 70 Wm^{-2} for Nimbus–7 and 100 Wm^{-2} for ERBE. This results, primarily, from changes in the SW cloud effect caused by seasonal variations in solar insolation. The global net effect of clouds is negative, as evidenced in Table 3, and varies from season to season. The difference in the net cloud effect between Nimbus–7 and ERBE data is roughly 1–2 Wm^{-2}.

5. Conclusions

The impact of clouds on the ERB was determined using Nimbus–7 ERB observations and coincident THIRS/TOMS derived cloudiness data. A technique was outlined to obtain seasonal clear sky fluxes, and the uncertainties of these derived fluxes were estimated to be about 8 Wm^{-2} for the LW and 10 Wm^{-2} for the SW fluxes. The uncertainty in the SW fluxes, however, may be somewhat high as a result of small sample sizes. When compared with the clear sky fluxes from ERBE the Nimbus–7 SW fluxes were biased high, on average, by 3–4 Wm^{-2} and the LW fluxes underestimated by 5–6 Wm^{-2}, except in areas of persistent cloud cover. The likely cause of this discrepancy was cloud contamination of the Nimbus–7 fluxes, although it also may be due, in part, to the biases inherent in the ERBE clear sky fluxes.

The quantity referred to in this study as cloud effect, defined as the difference between the clear sky flux and the total flux at the TOA, was used to provide a quantitative indication of the direct effect of clouds on the ERB. It was found that the SW cloud effect was primarily negative and most pronounced in regions of midlatitude stratus clouds and storm tracks, whereas the positive LW effect was greatest in areas of tropical convective-type clouds. These two opposing effects nearly cancel one another in the tropics resulting in a small negative effect. This reciprocal nature of the LW and SW fluxes in the tropics has been described in other ERB studies. In the

37

midlatitudes the SW cloud effect predominated, producing a large negative net effect. On a global scale, clouds appeared to cool the planet by producing a net negative effect on the ERB. This effect also displayed some seasonal fluctuation. When compared with the results from ERBE on a zonally and globally averaged basis the Nimbus–7 SW and LW cloud effects were about 5 Wm^{-2} and 6 Wm^{-2} smaller, respectively, resulting in a difference in the net effect of 1–2 Wm^{-2}. These differences are attributed to cloud contamination of the Nimbus–7 clear sky fluxes and possibly biases in the ERBE clear sky fluxes.

6. Acknowledgments

7. References

Ardanuy, P. E., L. L. Stowe, A. Gruber, M. Weiss, and C. S. Long, 1989: Longwave cloud radiative forcing as determined from Nimbus–7 observations. *J. Climate*, **2**, 766–799.

Ardanuy, P. E., L. L. Stowe, A. Gruber, M. Weiss, 1988: Shortwave, longwave, and net cloud-radiative forcing as determined from Nimbus–7 observations. *Proc. Int. Radiation Symposium*, 18–24 Aug., Lille, France, A. Deepak Publ., 134–138.

Arking, A., and S. Vermury, 1984: the NIMBUS 7 ERB data set: A critical analysis. *J. Geophys. Res.*, **89**, 5089–5097.

Barkstrom, B. R., 1984: The Earth Radiation Budget Experiment (ERBE). *Bull. Am. Meteor. Soc.*, **65**, 1170–1185.

Charlock, T. P., and V. Ramanathan, 1985: The albedo field and cloud radiative forcing produced by a general circulation model with internally generated cloud optics. *J. Atmos. Sci.*, **42**, 1408–1429.

Ellis, J. S., 1978: Cloudiness, the planetary radiation budget, and climate, Ph. D. dissertation, Colorado State Univ., 129 pp.

Harrison, E. F., P. Minnis, B. R. Barkstrom, V. Ramanathan, R. D. Cess, and G. G. Gibson, 1990: Seasonal variation of cloud radiative forcing derived from the Earth Radiation Budget Experiment. to appear in *J. Geophys. Res.*

Jacobowitz, H., H. V. Soule, H. L. Kyle, F. B. House, and the NIMBUS–7 ERB experiment team, 1984: The Earth Radiation Budget (ERB) experiment: An overview. *J. Geophys. Res.*, **89**, 5021-5038.

Ohring, G., A. Gruber, and R. Ellingson, 1984: Satellite determination of the relationship between total longwave flux and infrared window radiance. *J. Clim. and Appl. Meteor.*, **23**, 416–425.

Ramanathan, V., B. R. Barkstrom, and E. F. Harrison, 1989a: Climate and the earth's radiation budget. *Physics Today*, **42**, 22-32.

Ramanathan, V., R. D. Cess, E. F. Harrison, P. Minnis, B. R. Barkstrom, E. Ahmad, and D. Hartmann, 1989b: Radiative cloud forcing and climate: Results from the Earth Radiation Budget Experiment. *Science*, **243**, 57-63.

Ramanathan, V., 1987: The role of Earth Radiation Budget studies in climate and general circulation research. *J. Geophys. Res.*, **92**, 4075–4095.

Raschke, E., T. H. Vonder Haar, M. Pasternak, and W. R. Brandeen, 1973: The radiation balance of the earth-atmosphere system from Nimbus–3 radiation measurements. *NASA Tech. Note 7249*, 73 pp.

Schiffer, R. A., and W. B. Rossow, 1983: The International Satellite Cloud Climatology Project (ISCCP): The first project of the World Climate Research Programme, *Bull. Am. Meteor. Soc.*, **64**, 779–784.

Stowe, L. L., G. G. Wellemeyer, T. F. Eck, H. Y. M. Yeh, and the Nimbus–7 cloud data processing team, 1988: Nimbus–7 global cloud climatology. Part I: Algorithms and validation. *J. Climate*, **1**, 445-470.

Tighe R. J., and M. Y. H. Shen, 1984: Nimbus–7 Earth Radiation Budget (ERB) MATRIX user's guide, Volume I: Experiment description and quality control report for year 1. NASA contractor report CR-170619, 119 pp.